

An efficient formalism for inertial spin waves: Dzyaloshinskii-Moriya antiferromagnets as case studies

De-Yun Zhao¹, Ri-Xing Wang², Meng-Qiu Cai¹, Mikhail Cherkasskii³, Peng-Bin He¹

¹*School of Physics and Electronics, Hunan University, Changsha 410082, China*

²*College of Computer and Electrical Engineering,*

Hunan University of Arts and Science, Changde 415000, China

³*Institute for Theoretical Solid State Physics, RWTH Aachen University, DE-52074 Aachen, Germany*

(Dated: July 3, 2026)

Magnetic inertia, emerging in the ultrafast regime, supports inertial spin waves (SWs) as novel magnetic excitations. Despite considerable efforts devoted to inertial SWs, a systematic formalism for fully characterizing their intrinsic properties, especially chirality and polarization, is still lacking, and inertial SWs in spatially nonuniform magnetic configurations remain poorly explored. Here, we develop a framework for calculating inertial SWs and establish a general definition of their chirality and polarization via the ellipticity angle, a unified parameter encoding frequency sign, phase difference, and elliptical axis ratio. Using this method, we systematically investigate precessional and nutational SWs in uniaxial antiferromagnets with staggered and homogeneous Dzyaloshinskii-Moriya interactions (DMIs), covering uniform collinear, canted, and spiral magnetic configurations. The results reveal that small staggered DMI preserves spin-wave degeneracy, whereas small homogeneous DMI lifts it. Further space-time inversion symmetry breaking in canted and spiral structures fully removes spin-wave degeneracy across the entire Brillouin zone. Long-wavelength nutational SWs behave as backward waves, and flat bands emerge in canted and spiral configurations near a critical inertial relaxation time. In canted and spiral configurations, nutational modes are always lefthanded whereas precessional modes are always righthanded; additionally, the dispersion spectra of the canted configuration can be derived from those of the spiral configuration via band folding. Polarization is wavenumber insensitive for uniform configurations but becomes strongly dispersive for nonuniform ones. This work advances the fundamental understanding of magnetic inertial dynamics and provides theoretical insights for the development of ultrafast magnonic devices.

I. INTRODUCTION

Magnetic inertia [1], emerging in the context of ultrafast spin dynamics, has been experimentally confirmed via studies of magneto-inertial resonant excitations [2–4]. Theoretically, such magnetic inertia is incorporated into the Landau-Lifshitz-Gilbert (LLG) equation as a second-order time derivative term of magnetization. Several mechanisms have been proposed to explain the inertial term in the inertial LLG equation. Within the framework of mesoscopic non-equilibrium thermodynamics, magnetic inertia is obtained by extending the phase space of the magnetization to the degrees of freedom of the angular momentum [5]. Grounded in basic mechanical and electrodynamic principles, magnetic inertia emerges naturally from the fundamental proportionality between angular momentum and magnetization. [6]. Alternatively, a purely mechanical microscopic model (a circular current loop) can also yield the same inertial terms without presupposing this proportionality [7]. When memory effects arising from the noninstantaneous interaction between the magnetic system and its environment, such as electron and phonon baths, are taken into account on ultrafast time scales [8–17], the inertial term can be traced to the second-order contribution, in time or frequency, of the delayed environmental response. This contribution can be captured, for example, by an expansion of the memory kernel [8–13], a low-frequency expansion of the self-energy [14–16], or a high-frequency decomposi-

tion of bath modes [17]. According to the relativistic Dirac equation, spin inertia arises from the $1/c^4$ order spin-orbit coupling [18, 19]. Through Schwinger-Keldysh field theory, the optically induced magnetic inertia term is predicted [20].

Apart from exploring the origin of magnetic inertia, substantial efforts have been invested in the inertial magnetic dynamics. Significant magnetic nutation has been evidenced via exact analytic solutions of inertial Landau-Lifshitz equation [21], numerical simulations of the inertial LLG equation for several nanostructured systems [22], and time-dependent equilibrium correlation-function analyses [23]. Moreover, existing studies demonstrate that magnetic inertia gives rise to emergent nutational resonances alongside conventional ferromagnetic [24–31] and antiferromagnetic [32–34] ones. Besides these intrinsic inertial resonances, the interplay between nutational resonance and spin current has also been explored, covering nutation-injected spin pumping [35] and forced nutational resonance driven by spin torques [36]. Beyond the foregoing linear inertial magnetic dynamics, magnetic inertia also affects the nonlinear magnetic dynamics. Specifically, it alters the self-oscillation of magnetization in both antiferromagnets (AFMs) [37, 38] and ferromagnets (FMs) [39], and enables ultrafast magnetization switching [40–43]. In previously mentioned works, however, the polarization and chirality of resonant modes have received only limited attention. They are only briefly discussed in Ref. [30] and systematically explored for forced inertial resonance [36]. In addition, the chi-

rality is used to distinguish the spin pumping currents generated by nutational and precessional resonances [35].

The aforementioned theoretical studies have focused primarily on the temporal dynamics of magnetization, while works on inertial spin waves have additionally accounted for its spatial variation [44–53]. To the best of our knowledge, only a few studies have addressed spin-wave spectra across the entire Brillouin zone [49, 53], whereas most works remain restricted to the long-wavelength regime. With regards to the chirality, Ref. [46] points out that the magnetization precesses in opposite directions for the nutational and precessional SWs in ferromagnets. Furthermore, nearly all of these spin-wave analyses assume uniform ferromagnetic or antiferromagnetic ground states, while spin waves on top of nonuniform configurations appear to have been addressed only in very few works, for instance, the inertial SWs on a spin spiral [49].

While inertial SWs (and especially their dispersions) in uniform FMs and AFMs are well investigated, those in more complicated structures hosting spatially textured magnetization, such as canted and spiral configurations, are less explored. Moreover, a systematic characterization of the chirality and polarization of inertial SWs is still lacking, and the connection between spin-wave chirality and the sign of the eigenfrequency remains ambiguous. Therefore, we develop a more straightforward formalism for calculating inertial SWs, applicable to both uniform and nonuniform magnetic configurations. Furthermore, we propose a general definition of the chirality and polarization of SWs. The formalism is validated through a case study of uniaxial AFMs with staggered and homogeneous Dzyaloshinskii-Moriya interactions (DMIs).

This paper is structured as follows. Section II outlines the theoretical framework adopted throughout our analysis. Sec. III details the equilibrium configurations of uniaxial AFMs with staggered and homogeneous DMIs. In Sec. IV, we investigate inertial SWs in AFMs with staggered DMI, covering excitations built upon uniform AFM and canted equilibrium configurations. The inertial SWs for homogeneous-DMI AFMs are given in Sec. V, where we address SWs originating from uniform AFM and spiral ground states. Finally, some discussions and conclusions are presented in Secs. VI and VII, respectively. Some complicated intermediate formulas and derivations are provided in the Appendix.

II. METHODOLOGY

The discrete inertial Landau-Lifshitz (ILL) equation reads

$$\frac{\partial \mathbf{m}_l}{\partial t} = -\mathbf{m}_l \times \mathbf{h}_l^{eff} + \eta \mathbf{m}_l \times \frac{\partial^2 \mathbf{m}_l}{\partial t^2}, \quad (1)$$

where η is the inertial relaxation time, \mathbf{m}_l is the unit vector of the magnetization \mathbf{M}_l at l -th site. The effective

field \mathbf{h}_l^{eff} can be calculated by $\mathbf{h}_l^{eff} = -\partial E / \partial \mathbf{m}_l$, with the reduced magnetic energy E having the dimension of frequency; see for example Eq. (18).

Most static magnetic configurations are spatially nonuniform. To analyze SWs living on top of them, it is convenient to take the local sets of coordinates attached to the spatially varying equilibrium magnetization. The unit basis vectors of the local frame are defined as

$$\begin{pmatrix} \mathbf{e}_r^l \\ \mathbf{e}_\theta^l \\ \mathbf{e}_\phi^l \end{pmatrix} = \begin{pmatrix} \sin \theta_l^0 \cos \phi_l^0 & \sin \theta_l^0 \sin \phi_l^0 & \cos \theta_l^0 \\ \cos \theta_l^0 \cos \phi_l^0 & \cos \theta_l^0 \sin \phi_l^0 & -\sin \theta_l^0 \\ -\sin \phi_l^0 & \cos \phi_l^0 & 0 \end{pmatrix} \begin{pmatrix} \mathbf{e}_x \\ \mathbf{e}_y \\ \mathbf{e}_z \end{pmatrix}, \quad (2)$$

with θ_l^0 being the polar angle between \mathbf{m}_l^0 and the positive z -axis, and ϕ_l^0 being the azimuthal angle between the projection of \mathbf{m}_l^0 on the xy -plane and the x -axis. Here, \mathbf{m}_l^0 denotes the equilibrium direction of the magnetization at the l -th site and satisfies the torque-free condition $\mathbf{m}_l \times \mathbf{h}_l^{eff} |_{\mathbf{m}_l = \mathbf{m}_l^0} = 0$. By this definition and Eq. (2), $\mathbf{e}_r^l = \mathbf{m}_l^0$.

The spin-wave ansatz is assumed as

$$\mathbf{m}_l = \mathbf{m}_l^0 + \delta \mathbf{m}_l, \quad (3)$$

where $\delta \mathbf{m}_l$ is the dynamic components, which is small in the linear regime. In the local coordinate frame defined in Eq. (2), the spin-wave fluctuation can be expanded up to second order in the small quantities as

$$\delta \mathbf{m}_l \approx m_{\theta,l} \mathbf{e}_\theta^l + m_{\phi,l} \mathbf{e}_\phi^l - \frac{1}{2} (m_{\theta,l}^2 + m_{\phi,l}^2) \mathbf{e}_r^l, \quad (4)$$

with $m_{\theta(\phi),l}$ being the component of spin-wave fluctuation in $\mathbf{e}_{\theta(\phi)}^l$ direction. According to Eq. (4), the reduced energy is a function of $m_{\theta,l}$ and $m_{\phi,l}$. The effective field in the local frame can be calculated by

$$\mathbf{h}_l^{eff} = -\frac{\partial E}{\partial m_{\theta,l}} \mathbf{e}_\theta^l - \frac{\partial E}{\partial m_{\phi,l}} \mathbf{e}_\phi^l. \quad (5)$$

Remaining the zero-order and linear terms of $m_{\theta,l}$ and $m_{\phi,l}$, the effective field are expanded as

$$\mathbf{h}_l^{eff} = \mathbf{h}_l^0 + \delta \mathbf{h}_l, \quad (6)$$

where \mathbf{h}_l^0 is the effective field in equilibrium, and $\delta \mathbf{h}_l$ is the linear fluctuation of the effective field. The expressions of \mathbf{h}_l^0 and $\delta \mathbf{h}_l$ are presented in Appendix. A.

Substituting the spin-wave ansatz described by Eq. (3) and (4) and the effective field expansion Eq. (6) into the ILL equation (1), and utilizing the equilibrium equation $\mathbf{m}_l^0 \times \mathbf{h}_l^0 = 0$, one can get a set of differential equations

for $(m_{\theta,l}, m_{\phi,l})$ after linearization,

$$\frac{\partial}{\partial t} \begin{pmatrix} m_{\theta,l} \\ m_{\phi,l} \end{pmatrix} + \eta \Omega \frac{\partial^2}{\partial t^2} \begin{pmatrix} m_{\theta,l} \\ m_{\phi,l} \end{pmatrix} = -\Omega \times \left[\mathcal{H}_l \begin{pmatrix} m_{\theta,l} \\ m_{\phi,l} \end{pmatrix} + \mathcal{H}_{l+1} \begin{pmatrix} m_{\theta,l+1} \\ m_{\phi,l+1} \end{pmatrix} + \mathcal{H}_{l-1} \begin{pmatrix} m_{\theta,l-1} \\ m_{\phi,l-1} \end{pmatrix} \right], \quad (7)$$

where Ω is the symplectic unit matrix,

$$\Omega = \begin{pmatrix} 0 & 1 \\ -1 & 0 \end{pmatrix}. \quad (8)$$

The three \mathcal{H} matrixes read

$$\mathcal{H}_{l'} = \begin{pmatrix} \frac{\partial^2 E}{\partial m_{\theta,l} \partial m_{\theta,l'}} & \frac{\partial^2 E}{\partial m_{\theta,l} \partial m_{\phi,l'}} \\ \frac{\partial^2 E}{\partial m_{\phi,l} \partial m_{\theta,l'}} & \frac{\partial^2 E}{\partial m_{\phi,l} \partial m_{\phi,l'}} \end{pmatrix}_0, \quad (9)$$

where, the subscript '0' indicates that the derivatives are evaluated at the equilibrium state for $l' = l, l+1, l-1$. Here, the magnetic energy is restricted to nearest-neighbor interactions, giving rise to coupling between site l and its adjacent sites $l \pm 1$.

Eq. (7) constitutes a coupled system of linear second-order differential equations, which are generally site-dependent. Introducing the auxiliary phase-space variables $\partial m_{\theta,l}/\partial t$ and $\partial m_{\phi,l}/\partial t$, the original second-order system can be recast as a first-order one with doubled dimensionality. This reformulation significantly simplifies the evaluation of spin-wave eigenfrequencies and their corresponding eigenvectors. The resulting first-order differential equations can be written as

$$\frac{\partial \mathbf{v}_l}{\partial t} = -i\mathcal{M}_l \mathbf{v}_l - i\mathcal{M}_{l+1} \mathbf{v}_{l+1} - i\mathcal{M}_{l-1} \mathbf{v}_{l-1}. \quad (10)$$

After introducing two new dynamic variables, the vectors \mathbf{v}_l are defined as

$$\mathbf{v}_l = \left(m_{\theta,l}, m_{\phi,l}, i \frac{\partial m_{\theta,l}}{\partial t}, i \frac{\partial m_{\phi,l}}{\partial t} \right)^T, \quad (11)$$

with T denoting the transpose of matrix. Vectors $\mathbf{v}_{l \pm 1}$ are defined in the identical manner. The top half part of \mathbf{v}_l gives the linear SW. The parameter matrixes are also expanded as

$$\mathcal{M}_l = \begin{pmatrix} O_2 & I_2 \\ \frac{1}{\eta} \mathcal{H}_l & \frac{i}{\eta} \Omega \end{pmatrix}, \quad (12)$$

and

$$\mathcal{M}_{l \pm 1} = \begin{pmatrix} O_2 & O_2 \\ \frac{1}{\eta} \mathcal{H}_{l \pm 1} & O_2 \end{pmatrix}. \quad (13)$$

with O_2 and I_2 being the 2×2 zero matrix and identity

matrix, respectively.

Assuming the plane-wave solution, we have

$$\begin{pmatrix} m_{\theta,l} \\ m_{\phi,l} \end{pmatrix} = \begin{pmatrix} \mathcal{A}_{\theta,l} \\ \mathcal{A}_{\phi,l} \end{pmatrix} e^{-i\omega t + ikla}, \quad (14)$$

with k being the wave vector and a the lattice constant. $\mathcal{A}_{\theta(\phi),l}$ is the complex amplitude of $m_{\theta(\phi),l}$. $m_{\theta(\phi),l \pm 1}$ follows the same form. Inserting Eq. (14) into Eqs. (11) and (10) yields the spin-wave eigen-equation,

$$\widetilde{\mathcal{M}}_l \begin{pmatrix} \mathcal{A}_{\theta,l} \\ \mathcal{A}_{\phi,l} \\ \omega \mathcal{A}_{\theta,l} \\ \omega \mathcal{A}_{\phi,l} \end{pmatrix} = \omega \begin{pmatrix} \mathcal{A}_{\theta,l} \\ \mathcal{A}_{\phi,l} \\ \omega \mathcal{A}_{\theta,l} \\ \omega \mathcal{A}_{\phi,l} \end{pmatrix}, \quad (15)$$

where $\widetilde{\mathcal{M}}_l = \mathcal{M}_l + e^{ika} \mathcal{M}_{l+1} + e^{-ika} \mathcal{M}_{l-1}$. Eq. (15) and its matrixes Eqs. (12), (13) and (9) constitute the core of our method. The solution of this system provides the inertial spin-wave modes associated for various uniform and nonuniform magnetic configurations.

After getting the explicit expressions of $\mathcal{A}_{\theta,l}$ and $\mathcal{A}_{\phi,l}$, the precessional trajectories of magnetization can be reconstructed from Eq. (14) by taking the real part of $m_{\theta,l}(t)$ and $m_{\phi,l}(t)$. The plane-wave solution of SW reads

$$m_{\theta(\phi),l} = A_{\theta(\phi),l} \cos(-\omega t + kla + \delta_{\theta(\phi),l}). \quad (16)$$

In Eq. (16), $A_{\theta(\phi),l}$ denotes the real amplitude derived from the modulus of $\mathcal{A}_{\theta(\phi),l}$, while $\delta_{\theta(\phi),l}$ represents the initial phase corresponding to the argument of $\mathcal{A}_{\theta(\phi),l}$.

Here, we define the chirality as the rotational sense of \mathbf{m}_l around its equilibrium magnetization, i.e. $\mathbf{e}_r^l = \mathbf{m}_l^0$. It is convenient to represent both the chirality and polarization of a SW by using a single parameter, known as the ellipticity angle [54], which is defined as

$$\sin 2\chi_l = \text{sgn}(\omega) \frac{2A_{\theta,l}A_{\phi,l}}{A_{\theta,l}^2 + A_{\phi,l}^2} \sin \delta, \quad (17)$$

where $\delta = \delta_{\phi,l} - \delta_{\theta,l}$ denotes the phase difference and $\text{sgn}(\omega) = \omega/|\omega|$. The ellipticity angle is restricted to the interval $\chi_l \in [-\pi/4, \pi/4]$. For $|\chi| = 0$, the spin wave is linearly polarized, with the polarization direction lying anywhere in the local transverse plane, including along the \mathbf{e}_θ or \mathbf{e}_ϕ axes as special cases. For $|\chi_l| = \pi/4$, the SW is circularly polarized. For $0 < |\chi| < \pi/4$, the SW is elliptically polarized. As $|\chi|$ increases, the polarization approaches more circular. For positive (negative) χ , the chirality is righthanded (lefthanded). It should be emphasized that only the sign of ω can not determine the chirality of a SW, which also depends on the phase difference δ between two dynamic components of magnetization. Of course, flipping the sign of ω results in the reversal of chirality if $\sin \delta$ preserves its sign.

To demonstrate the robustness of the proposed formalism, we apply it to calculate the dispersion relation,

polarization, chirality, and phase of inertial SWs. The studied systems are uniaxial antiferromagnets with both homogeneous and staggered DMI, hosting either uniform or textured magnetic configurations. We first define their equilibrium configurations.

III. EQUILIBRIUM CONFIGURATIONS

The magnetic energy under consideration accounts for the contributions from the exchange interaction, the uniaxial magnetic anisotropy, and the DMI. Expressed in the frequency unit, the reduced magnetic energy reads

$$E = \sum_l \left[\omega_E \mathbf{m}_l \cdot \mathbf{m}_{l+1} - \omega_K (\mathbf{m}_l \cdot \mathbf{e}_z)^2 + \lambda \omega_D \mathbf{e}_z \cdot (\mathbf{m}_l \times \mathbf{m}_{l+1}) \right], \quad (18)$$

where $\omega_E = \gamma J / (\mu_0 M)$, $\omega_K = \gamma K / (\mu_0 M)$, and $\omega_D = \gamma D / (\mu_0 M)$, with $J > 0$ being the exchange energy density between the nearest local magnetic moments, K the easy-axis anisotropy constant, D the DM constant, and M the magnitude of \mathbf{M}_l . The choice $\lambda = 1$ corresponds to homogeneous DMI, whereas $\lambda = (-1)^l$ describes staggered DMI [55–59]. Here, it is assumed that the easy axis and the DM vector are along the z -axis. Comparing with the homogeneous DMI, only an additional factor $(-1)^l$ appears in the staggered DMI term. This modification implies that the staggered DM vectors for neighboring magnetic moments align in opposite directions.

Minimizing the magnetic energy [eq. (18)] determines the static magnetic configuration. In equilibrium, the system adopts the AFM configuration shown in Fig. 1(a) when $|\omega_D| < \omega_D^c$. The critical value of ω_D reads

$$\omega_D^c = \sqrt{\omega_K(2\omega_E + \omega_K)}. \quad (19)$$

When $|\omega_D| > \omega_D^c$, the system twists into a spiral state for homogeneous DMI [57, 59], as shown in Fig. 1(b), whereas for staggered DMI [57–59] it enters the canted configuration shown in Fig. 1(c). In the absence of anisotropy, one obtains $\omega_D^c = 0$, such that homogeneous DMI immediately drives the system into a spiral state, whereas staggered DMI gives rise to a canted configuration.

The spiral state is described by $m_l^z = 0$, $m_l^x = \cos(l\phi_s)$, $m_l^y = \sin(l\phi_s)$, with spin rotation angle per lattice step

$$\phi_s = \tan^{-1}(-\omega_E, -\omega_D), \quad (20)$$

where $\tan^{-1}(x, y)$ denotes the two-argument arctangent that returns the angle of the vector (x, y) , correctly resolving the quadrant [60]. Evidently, for $\omega_E > 0$, ϕ_s is close to a straight angle owing to $\omega_D \ll \omega_E$.

The canted state is double degenerate, described by $m_l^z = 0$, $m_{2j+1}^x = -m_{2j}^x = \pm \cos(\phi_c)$, $m_{2j+1}^y = m_{2j}^y =$

$\pm \sin(\phi_c)$, with the canted angle

$$\phi_c = \frac{1}{2} \tan^{-1}(\omega_E, \omega_D). \quad (21)$$

Based on the foregoing AFM, spiral and canted configurations, we proceed to compute the SWs below.

IV. INERTIAL SPIN WAVES IN AFM WITH STAGGERED DMI

A. Spin waves on top of AFM configuration

When $\omega_D < \omega_D^c$, the AFM configuration serves as the equilibrium state. We derive the spin-wave solutions using the approach introduced in Sec. II, with the detailed derivations provided in Appendix B. For two sublattices, Eq. (16) is recast as

$$m_{\theta(\phi), 2j} = A_{\theta(\phi), 2j} \cos[-\omega t + 2jka + \delta_{\theta(\phi), 2j}], \quad (22)$$

$$m_{\theta(\phi), 2j+1} = A_{\theta(\phi), 2j+1} \cos[-\omega t + (2j+1)ka + \delta_{\theta(\phi), 2j+1}]. \quad (23)$$

In this case, DMI fails to lift the degeneracy. The spin-wave spectrum consists of four branches: two positive-frequency branches and their two negative-frequency counterparts. Each branch is doubly degenerate. Hence, numerous solutions can be constructed through distinct linear combinations of degenerate mode pairs. In particular, circularly polarized SWs have been extensively investigated [61]. By linearly superposing the degenerate modes, we obtain such circularly polarized SWs. Their amplitudes and initial phases, as well as the ellipticity angles [calculated from Eq. (17)] are listed in Tab. I for every branches of SWs. To better clarify these characteristics, we illustrate the precessional trajectories of the magnetization tip for all modes of the two sublattices in Tab. II. This schematic clearly presents their chirality, amplitude ratios and phase differences. Additionally, we plot the dispersions and the dependence of sublattice amplitude ratios on the wave number in Fig. 2.

In Tab. I, the eigenfrequencies of nutational and precessional SWs read

$$\omega_{n,p} = \frac{\sqrt{1 + \eta\Gamma \pm \sqrt{(1 + \eta\Gamma)^2 - \eta^2\Lambda^2}}}{\sqrt{2}\eta}, \quad (24)$$

where $\Gamma = 4\sqrt{\omega_E^2 + \omega_D^c^2}$, and $\Lambda = 4[(\omega_E^2 + \omega_D^c^2) - (\omega_E^2 + \omega_D^2) \cos^2 ka]^{1/2}$. In Eq. (24), the subscripts n, p refer, respectively, to the upper and lower signs of \pm in front of the square root. In the limit that $\eta \rightarrow 0$, ω_n approaches infinity, and ω_p becomes $2[(\omega_E^2 + \omega_D^c^2) - (\omega_E^2 + \omega_D^2) \cos^2 ka]^{1/2}$. Notably, Λ is purely imaginary for some values of k when $\omega_D > \omega_D^c$, yielding $\Lambda^2 < 0$. Consequently, ω_p becomes complex according to Eq. (24), indicating the instability of AFM configuration.

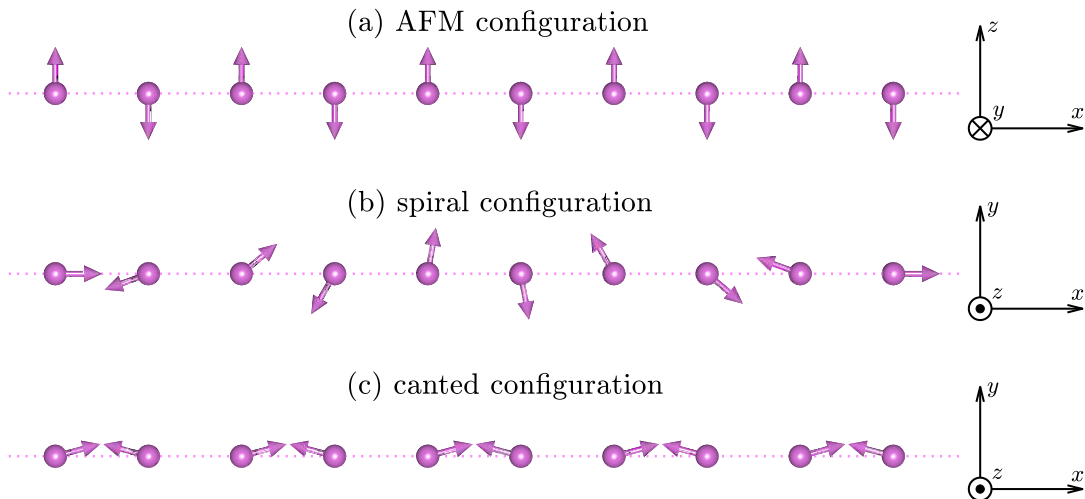


FIG. 1. (color online). The static magnetic configurations of AFMs with homogeneous and staggered DMIs.

TABLE I. Amplitudes, phases, and ellipticity angles of the SWs on top of an AFM configuration for staggered DMI. Here, $H(\lambda)$ is the unit step function and $\lambda = \text{sgn}(\cos ka)$. To better compare the amplitude ratio between two sublattices, all the amplitudes of mode II of nutation (precession) are multiplied by $|\rho_n|/|\rho_p|$. Here, $\varphi_0 = \arctan(\omega_E, \omega_D)$.

	ω_n		$-\omega_n$		ω_p		$-\omega_p$	
	mode I	mode II	mode I	mode II	mode I	mode II	mode I	mode II
$A_{\theta,2j}$	$\frac{ \rho_n }{\omega_n}$	$\frac{1}{\omega_n}$	$\frac{ \rho_n }{\omega_n}$	$\frac{1}{\omega_n}$	$\frac{ \rho_p }{\omega_p}$	$\frac{1}{\omega_p}$	$\frac{ \rho_p }{\omega_p}$	$\frac{1}{\omega_p}$
$A_{\phi,2j}$	$\frac{ \rho_n }{\omega_n}$	$\frac{1}{\omega_n}$	$\frac{ \rho_n }{\omega_n}$	$\frac{1}{\omega_n}$	$\frac{ \rho_p }{\omega_p}$	$\frac{1}{\omega_p}$	$\frac{ \rho_p }{\omega_p}$	$\frac{1}{\omega_p}$
$\delta_{\theta,2j}$	$\pi H(-\lambda) - \varphi_0$	$\pi H(\lambda) + \varphi_0$	$\pi H(-\lambda) + \varphi_0$	$\pi H(\lambda) - \varphi_0$	$\pi H(-\lambda) + \varphi_0$	$\pi H(\lambda) - \varphi_0$	$\pi H(-\lambda) - \varphi_0$	$\pi H(\lambda) + \varphi_0$
$\delta_{\phi,2j}$	$\lambda \frac{\pi}{2} - \varphi_0$	$\lambda \frac{\pi}{2} + \varphi_0$	$-\lambda \frac{\pi}{2} + \varphi_0$	$-\lambda \frac{\pi}{2} - \varphi_0$	$-\lambda \frac{\pi}{2} + \varphi_0$	$-\lambda \frac{\pi}{2} - \varphi_0$	$\lambda \frac{\pi}{2} - \varphi_0$	$\lambda \frac{\pi}{2} + \varphi_0$
$A_{\theta,2j+1}$	$\frac{1}{\omega_n}$	$\frac{ \rho_n }{\omega_n}$	$\frac{1}{\omega_n}$	$\frac{ \rho_n }{\omega_n}$	$\frac{1}{\omega_p}$	$\frac{ \rho_p }{\omega_p}$	$\frac{1}{\omega_p}$	$\frac{ \rho_p }{\omega_p}$
$A_{\phi,2j+1}$	$\frac{1}{\omega_n}$	$\frac{ \rho_n }{\omega_n}$	$\frac{1}{\omega_n}$	$\frac{ \rho_n }{\omega_n}$	$\frac{1}{\omega_p}$	$\frac{ A_p }{\omega_p}$	$\frac{1}{\omega_p}$	$\frac{ \rho_p }{\omega_p}$
$\delta_{\theta,2j+1}$	0	π	0	π	π	0	π	0
$\delta_{\phi,2j+1}$	$-\frac{\pi}{2}$	$-\frac{\pi}{2}$	$\frac{\pi}{2}$	$\frac{\pi}{2}$	$-\frac{\pi}{2}$	$-\frac{\pi}{2}$	$\frac{\pi}{2}$	$\frac{\pi}{2}$
χ_{2j}	$\frac{\pi}{4}$	$-\frac{\pi}{4}$	$\frac{\pi}{4}$	$-\frac{\pi}{4}$	$-\frac{\pi}{4}$	$\frac{\pi}{4}$	$-\frac{\pi}{4}$	$\frac{\pi}{4}$
χ_{2j+1}	$-\frac{\pi}{4}$	$\frac{\pi}{4}$	$-\frac{\pi}{4}$	$\frac{\pi}{4}$	$\frac{\pi}{4}$	$-\frac{\pi}{4}$	$\frac{\pi}{4}$	$-\frac{\pi}{4}$

In Tab. I, the parameters $\rho_{n,p}$ are given by

$$\rho_{n,p} = \pm \frac{2\sqrt{\omega_E^2 + \omega_D^2} \cos ka}{\eta\omega_{n,p}^2 \pm \omega_{n,p} - 2\sqrt{\omega_E^2 + \omega_D^2}}, \quad (25)$$

with the upper and lower signs of \pm corresponding to the subscripts n and p of $\rho_{n,p}$. It can be verified that $\eta\omega_n^2 + \omega_n - 2\sqrt{\omega_E^2 + \omega_D^2} > 0$ and $-(\eta\omega_p^2 - \omega_p - 2\sqrt{\omega_E^2 + \omega_D^2}) > 0$. So, the signs of $\rho_{n,p}$ are determined by $\cos(ka)$.

1. Dispersion

Near $k = 0$, the dispersions expanded to second order in k read

$$\omega_{n,p} = \sqrt{\Delta_{n,p}^2 \pm v^2 k^2}, \quad (26)$$

with the sign \pm before v^2 corresponding to the subscripts n and p of $\omega_{n,p}$. At $k = 0$, the frequency of the nutational SW reaches its maximum, as shown in Fig. 2(a), indicating the optical-branch character of this mode. The frequency maximum of the nutational branch (Δ_n) and

TABLE II. Schematic diagrams of the modes. The blue solid (red dotted) circles denote the trajectories of the tips of \mathbf{m}_{2j} (\mathbf{m}_{2j+1}). The arrows on the blue solid (red dotted) circles signify the rotational senses of \mathbf{m}_{2j} (\mathbf{m}_{2j+1}) around $-\mathbf{r}_r^{2j}$ (\mathbf{e}_r^{2j+1}). The blue solid (red dotted) vector line represent the fluctuation $\delta\mathbf{m}_{2j}$ ($\delta\mathbf{m}_{2j+1}$).

	ω_n		$-\omega_n$		ω_p		$-\omega_p$	
	mode I	mode II	mode I	mode II	mode I	mode II	mode I	mode II
$0 < k a < \frac{\pi}{2}$								
$\frac{\pi}{2} < k a < \pi$								
frame								

the gap of the precessional branch (Δ_p) are given by

$$\Delta_{n,p} = \frac{\sqrt{1 + \eta\Gamma \pm \sqrt{(1 + \eta\Gamma)^2 - 16\eta^2(\omega_D^c - \omega_D^2)}}}{\sqrt{2}\eta}, \quad (27)$$

where the subscripts n and p refer, respectively, to the upper and lower signs in front of the square root. The precessional spin-wave gap Δ_p is reduced by the spin inertia, as can be seen from the expansion:

$$\Delta_p = 2\sqrt{\omega_D^c - \omega_D^2} [1 - \Gamma\eta + O(\eta^2)]. \quad (28)$$

When $\omega_D = \omega_D^c$, the gap vanishes; when $\omega_D > \omega_D^c$, Δ_p becomes complex, leading to the instability of these SWs.

The characteristic velocity v in Eq. (26) is

$$v = \frac{2\sqrt{\omega_E^2 + \omega_D^2}a}{\left[(1 + \eta\Gamma)^2 - 16\eta^2(\omega_D^c - \omega_D^2)\right]^{\frac{1}{4}}}, \quad (29)$$

which is identical for the nutational and precessional SWs. From Eq. (29), it can be inferred that the presence of spin inertia diminishes the velocity. Obviously, the group velocity of the nutational SW has the opposite sign to the wave number k , which classifies it as a backward SW.

At $k = \pm\pi/(2a)$, the nutational spin-wave branch reaches the bottom of its dispersion band, whereas the precessional spin-wave branch reaches the top of its band. The frequencies at the bottom of nutational band and the top of precessional band read

$$\omega_{n(p)}^{b(t)} = \frac{\sqrt{1 + 8\eta(\omega_E + \omega_K)} \pm 1}{2\eta}, \quad (30)$$

where \pm signs correspond to ω_n^b and ω_p^t respectively.

Then, the gap between nutational and precessional bands is $1/\eta$, which is suppressed with increasing η .

2. Sublattice amplitude ratio

The amplitude ratio of SWs between two sublattices can be represented by $|\rho_{n,p}|$, which varies with k , as displayed in Fig. 2(b). At $k = 0$, the sublattice amplitude ratios reach their maximum values. In particular, the ratio is close to 1 for the precessional mode. Under the conditions $\omega_K \ll \omega_E$ and $\omega_D \ll \omega_E$, $|\rho_p|$ reduces to

$$\rho_p^0 \approx 1 - \frac{1}{2} \frac{1}{1 + 4\eta\omega_E} \frac{\omega_D^2}{\omega_E^2} - \sqrt{2} \frac{1}{\sqrt{1 + 4\eta\omega_E}} \times \left(1 - \frac{\omega_D^2}{4\omega_E\omega_K}\right) \sqrt{\frac{\omega_K}{\omega_E}}, \quad (31)$$

which remains close to unity because both ω_K and ω_D are small compared with ω_E . This indicates that the amplitudes of precessional modes in two sublattices, in the long-wavelength limit, are almost identical. With increasing k from $k = 0$, $|\rho_{n,p}|$ decreases gradually and vanishes at $k = \pi/(2a)$. This implies that, for short-wavelength SWs with $\lambda = 4a$, the excitation is localized on a single sublattice. In addition, the sublattice amplitude ratios of mode I and mode II are mutually reciprocal, as clearly seen from the A_θ and A_ϕ data presented in Tab. I. This feature is also illustrated schematically in Tab. II.

3. Chirality and phase

Since we adopt local coordinate frames (shown in Tab. II) throughout spin-wave calculations, chirality is defined as the rotational sense about the equilibrium magnetization of each individual sublattice [63]. Following this def-

TABLE III. Amplitudes, phases, and ellipticity angles of the SWs on top of a canted configuration for staggered DMI.

	ω_n^+	$-\omega_n^+$	ω_n^-	$-\omega_n^-$	ω_p^+	$-\omega_p^+$	ω_p^-	$-\omega_p^-$
$A_{\theta,2j}$	ρ_n^+	ρ_n^+	ρ_n^-	ρ_n^-	ρ_p^+	ρ_p^+	ρ_p^-	ρ_p^-
$A_{\phi,2j}$	$\frac{1}{\omega_n^+}$	$\frac{1}{\omega_n^+}$	$\frac{1}{\omega_n^-}$	$\frac{1}{\omega_n^-}$	$\frac{1}{\omega_p^+}$	$\frac{1}{\omega_p^+}$	$\frac{1}{\omega_p^-}$	$\frac{1}{\omega_p^-}$
$\delta_{\theta,2j}$	0	0	π	π	π	π	0	0
$\delta_{\phi,2j}$	$-\frac{\pi}{2}$	$\frac{\pi}{2}$	$\frac{\pi}{2}$	$-\frac{\pi}{2}$	$-\frac{\pi}{2}$	$\frac{\pi}{2}$	$\frac{\pi}{2}$	$-\frac{\pi}{2}$
$A_{\theta,2j+1}$	ρ_n^+	ρ_n^+	ρ_n^-	ρ_n^-	ρ_p^+	ρ_p^+	ρ_p^-	ρ_p^-
$A_{\phi,2j+1}$	$\frac{1}{\omega_n^+}$	$\frac{1}{\omega_n^+}$	$\frac{1}{\omega_n^-}$	$\frac{1}{\omega_n^-}$	$\frac{1}{\omega_p^+}$	$\frac{1}{\omega_p^+}$	$\frac{1}{\omega_p^-}$	$\frac{1}{\omega_p^-}$
$\delta_{\theta,2j+1}$	π	π	π	π	0	0	0	0
$\delta_{\phi,2j+1}$	$\frac{\pi}{2}$	$-\frac{\pi}{2}$	$\frac{\pi}{2}$	$-\frac{\pi}{2}$	$\frac{\pi}{2}$	$-\frac{\pi}{2}$	$\frac{\pi}{2}$	$-\frac{\pi}{2}$
χ_{2j}	$-X_n^+$	$-X_n^+$	$-X_n^-$	$-X_n^-$	X_p^+	X_p^+	X_p^-	X_p^-
χ_{2j+1}	$-X_n^+$	$-X_n^+$	$-X_n^-$	$-X_n^-$	X_p^+	X_p^+	X_p^-	X_p^-

initiation, modes I and II exhibit opposite signs of χ with $|\chi| = \pi/4$, indicating opposite chiralities that correspond to left-handed and right-handed circular polarizations, respectively. Moreover, the corresponding chirality exhibits an opposite orientation between two sublattices. By contrast, some previous studies choose the magnetic field direction, aligned with the static magnetization of one sublattice, as the rotational axis. With this alternative convention, the two sublattices have the same chirality.

Here, flipping the sign of frequency can not reverse the chirality of SWs. As seen by comparing the phase characteristics of the $\omega_{n,p}$ -branch with those of the corresponding $-\omega_{n,p}$ -branch in Table I, the phase differences between the \mathbf{e}_θ and \mathbf{e}_ϕ components of the spin-wave fluctuations have opposite signs. According to the definition of ellipticity angle Eq. (17), the chirality is not altered when combining with the sign reversal of ω .

Additionally, in Tab. II, we schematically illustrate the phases of all modes at a specific lattice site at a given instant in time. It reveals that, for $0 < ka < \pi/2$, the two sublattices oscillate with a phase difference of φ_0 for nutation and with a phase difference of $\pi + \varphi_0$ for precession; for $\pi/2 < ka < \pi$, the phase relations are reversed. Without DMI, φ_0 is zero.

B. Spin waves on top of canted configuration

When $\omega_D > \omega_D^c$, the canted configuration is preferred in equilibrium. After calculating the spin-wave modes, as detailed in Appendix C, the components of the spin-wave fluctuations can be expressed in the form of Eqs. (22) and (23). In this case, the spectrum is nondegenerate. Eight spin-wave branches are obtained, four with positive frequencies and four corresponding negative-frequency branches. Their amplitudes and initial phases, as well as the ellipticity angles [calculated from Eq. (17)] are listed in Tab. III for every branches of SWs. Additionally,

we plot the dispersions and the dependence of ellipticity angles on the wave number in Fig. 3.

In Tab III, the eigenfrequencies of nutational and precessional SWs read

$$\omega_{n,p}^\pm(k) = \frac{\sqrt{1 + \eta\Gamma_\pm \pm \sqrt{(1 + \eta\Gamma_\pm)^2 - \eta^2\Lambda_\pm^2}}}{\sqrt{2}\eta}, \quad (32)$$

where $\Gamma_\pm = 2(f_\pm + g_\pm)$, and $\Lambda_\pm = 4\sqrt{f_\pm g_\pm}$, with $f_\pm(k) = \sqrt{\omega_E^2 + \omega_D^2} - \sqrt{\omega_E^2 + \omega_D^2} + \omega_E(1 \mp \cos ka)$, and $g_\pm(k) = \sqrt{\omega_E^2 + \omega_D^2}(1 \pm \cos ka)$. In Eq. (32), the subscripts n, p refer, respectively, to the upper and lower signs of \pm in front of the square root. It's worth noting that $f_\pm(k)$ remains positive for any k if $\omega_D > \omega_D^c$. By contrast, when $\omega_D < \omega_D^c$, $f_\pm(k)$ becomes negative for some values of k , yielding $\Lambda_\pm^2 < 0$. This in turn implies that ω_p^\pm is complex according to Eq. (32), signifying the instability of canted configuration.

In Tab III, the parameters $\rho_{n,p}^\pm$ are given by

$$\rho_{n,p}^\pm = \pm \frac{1}{\eta(\omega_{n,p}^\pm)^2 - 2f_\pm}, \quad (33)$$

with the upper and lower signs in front of the fraction corresponding to the subscripts n and p of $\rho_{n,p}^\pm$, respectively. It can be verified that $\rho_{n,p}^\pm > 0$.

1. Long-wavelength regime

In the long-wavelength limit, the ω_n^+ - and ω_p^+ -branches can be described by

$$\omega_{n,p}^+ = \sqrt{\Delta_{n,p}^{+2} \mp v_{n,p}^{+2} k^2}, \quad (34)$$

with the upper and lower signs of \mp corresponding to the n and p branches, respectively. In Eq. (34), the uniform

precession frequency

$$\Delta_{n,p}^+ = \frac{\sqrt{1 + 2\eta\xi \pm \sqrt{(1 + 2\eta\xi)^2 - 32\eta^2\tilde{\omega}_E\xi_-}}}{\sqrt{2}\eta}, \quad (35)$$

and the characteristic velocity

$$v_{n,p}^+ = a \sqrt{\frac{\zeta_- \left[1 \pm \sqrt{(1 + 2\eta\xi)^2 - 32\eta^2\tilde{\omega}_E\xi_-} \right] + 2\eta\zeta_+\xi_+}{2\eta\sqrt{(1 + 2\eta\xi)^2 - 32\eta^2\tilde{\omega}_E\xi_-}}}, \quad (36)$$

with $\tilde{\omega}_E = \sqrt{\omega_E^2 + \omega_D^2}$, $\xi = 3\sqrt{\omega_E^2 + \omega_D^2} - \sqrt{\omega_E^2 + \omega_D^2}$, $\xi_{\pm} = \sqrt{\omega_E^2 + \omega_D^2} \pm \sqrt{\omega_E^2 + \omega_D^2}$, and $\zeta_{\pm} = \sqrt{\omega_E^2 + \omega_D^2} \pm$

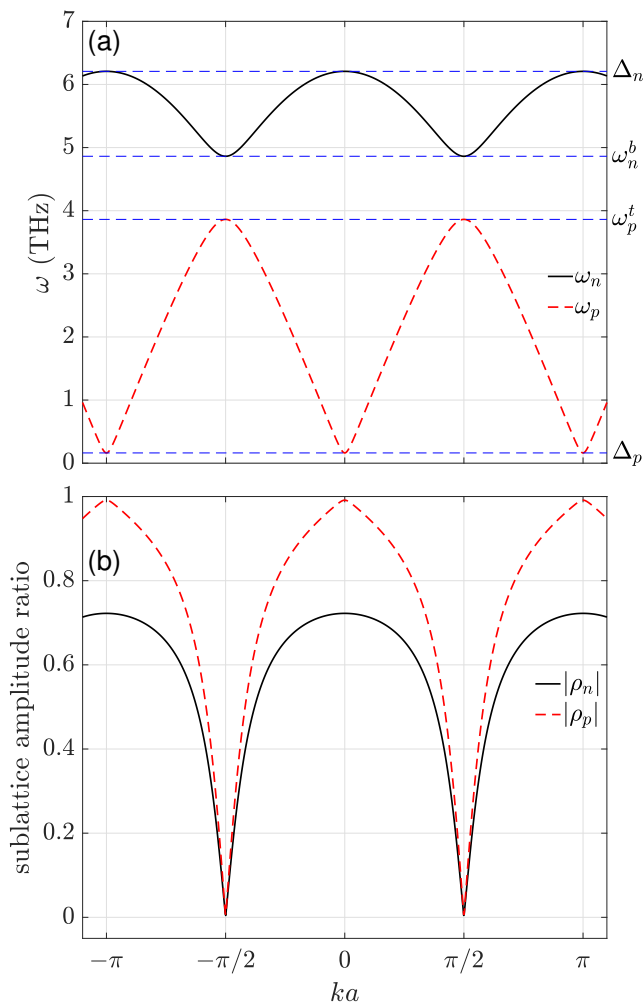


FIG. 2. (color online). Dispersion (a) and sublattice amplitude ratio (b) of the SWs on top of an AFM configuration for the case of staggered DMI. Here, $\omega_E = 9.25$ THz, and $\omega_K = 0.14$ THz, which are derived from the magnetic parameters of MnF₂ [62]. The inertial relaxation time η is set to 1 ps. ω_D is taken as $\frac{19}{20}\omega_D^c$, where $\omega_D^c \approx 1.62$ THz is evaluated from Eq. (19).

ω_E . In Eqs. (35) and (36), the upper and lower signs in front of the square root correspond to the n and p branches, respectively. In this case, the group velocity and wave number have opposite signs for the nutational SWs, which is a characteristic feature of backward SWs.

The ω_p^- -branch is gapless, as shown in Figs. 3(a) and 3(c). Its dispersion can be approximated as:

$$\omega_p^- = v_p^- |k|, \quad (37)$$

where

$$v_p^- = a \sqrt{\frac{2\sqrt{\omega_E^2 + \omega_D^2} (2\omega_E + \xi_-)}{1 + 2\eta(2\omega_E + \xi_-)}}. \quad (38)$$

The presence of spin inertia diminishes the velocity of long-wavelength SW. It should be mentioned that a Goldstone mode exists for the precessional SWs in the canted configuration, in contrast to the gapped SWs in the AFM configuration [see Fig. 2(a)]. This difference arises because the canted configuration breaks the rotational symmetry about the z axis, whereas the AFM configuration preserves this symmetry.

Comparison of the dotted curves in Figs. 3(a) and 3(c) shows that the long-wavelength dispersion of the ω_n^- branch differs substantially between the $\eta > \eta_c$ and $\eta < \eta_c$ regimes. The critical value η_c is derived as

$$\eta_c = \frac{1}{2\omega_E} \frac{\sqrt{\omega_E^2 + \omega_D^2} - \omega_E}{\sqrt{\omega_E^2 + \omega_D^2} - \sqrt{\omega_E^2 + \omega_D^2} + 2\omega_E}. \quad (39)$$

The dispersions for $\eta > \eta_c$ and $\eta < \eta_c$ can be written as a single equation,

$$\omega_n^- = \sqrt{(\Delta_n^-)^2 - \text{sgn}\left(1 - \frac{\eta_c}{\eta}\right) (v_n^-)^2 k^2}, \quad (40)$$

where

$$\Delta_n^- = \frac{\sqrt{1 + 2\eta(2\omega_E + \xi_-)}}{\eta}, \quad (41)$$

and

$$v_n^- = a \sqrt{\frac{2\omega_E(2\omega_E + \xi_-)}{1 + 2\eta(2\omega_E + \xi_-)} \left| 1 - \frac{\eta_c}{\eta} \right|}. \quad (42)$$

The velocity v_n^- becomes zero at $\eta = \eta_c$. Accordingly, the nutational dispersion is nearly flat in the long-wavelength regime, giving rise to a sharp peak for the density of states, and yielding strong and narrow signals for the specific heat and neutron scattering spectra.

Fig. 3(c) also indicates that the two nutational branches exhibit opposite dispersion behaviors for $\eta < \eta_c$: one reaches its maximum frequency at $k = 0$ (with minima at $k = \pm\pi/a$), while the other shows the opposite trend, attaining its minimum frequency at $k = 0$ and maxima at $k = \pm\pi/a$.

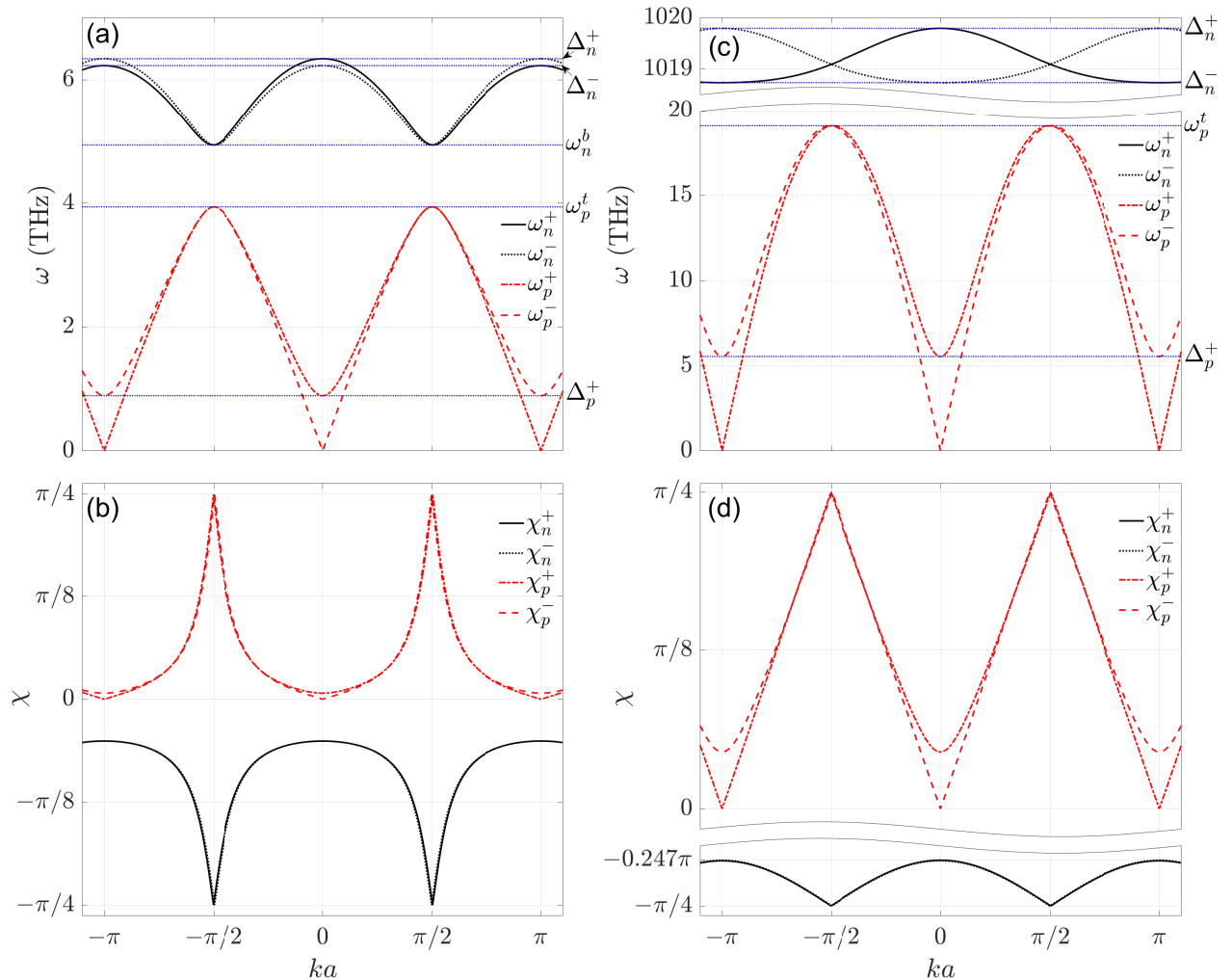


FIG. 3. Dispersions (a), (c) and ellipticity angles (b), (d) of the SWs on top of a canted configuration for the case of staggered DMI. (a) and (b) correspond to the regime $\eta > \eta_c$, while (c) and (d) are obtained for $\eta < \eta_c$. In (b) and (d), $\chi_n^\pm = -X_n^\pm$ and $\chi_p^\pm = X_p^\pm$. Here, $\eta = 1$ ps for (a) and (b), and $\eta = 1$ fs for (c) and (d). The DMI strength is set to $\omega_D = 2\omega_D^c$. The other parameters follow those adopted in Fig. 2.

2. Short-wavelength regime

It is interesting to examine the behaviors of SWs near $k = \pm\pi/(2a)$, as highlighted in the magnified plot of Fig. 4. At $k = \pm\pi/(2a)$, frequency degeneracy emerges separately for the two precessional branches and the two nutational branches, marking the unique degeneracy position for both types of excitations. At $k = k_p^\pm = (\pi/2 \pm \varphi_p)/a$, both precessional dispersion curves attain their maximum frequencies, with identical upper cutoff frequencies for the two branches. Similarly, the minimal frequencies of the two nutational dispersion curves are reached at $k = k_n^\pm = (\pi/2 \pm \varphi_n)/a$, again with identical cutoff

frequencies. The values of $\varphi_{n,p}$ are given by

$$\varphi_{n,p} = \arcsin \left\{ \frac{1}{\zeta_+} \left[\omega_K \pm \frac{1}{2\eta} \frac{\zeta_-}{\zeta_+} \times \frac{\sqrt{\omega_E + 2\eta\zeta_+ (2\omega_E + \xi_-)} \pm \sqrt{\omega_E}}{\sqrt{\omega_E}} \right] \right\}, \quad (43)$$

where the subscripts n and p correspond to the upper and lower signs of \pm , respectively. The quantities ζ_\pm and ξ_- are defined below Eq. (36). For typical experimental parameters, $\varphi_{n,p}$ is small, making it difficult to distinguish $k_{n,p}^+$ and $k_{n,p}^-$ in Fig. 3. To resolve this small separation, an enlarged view is shown in Fig. 4. The bottom of the nutational dispersion and the top of the precessional

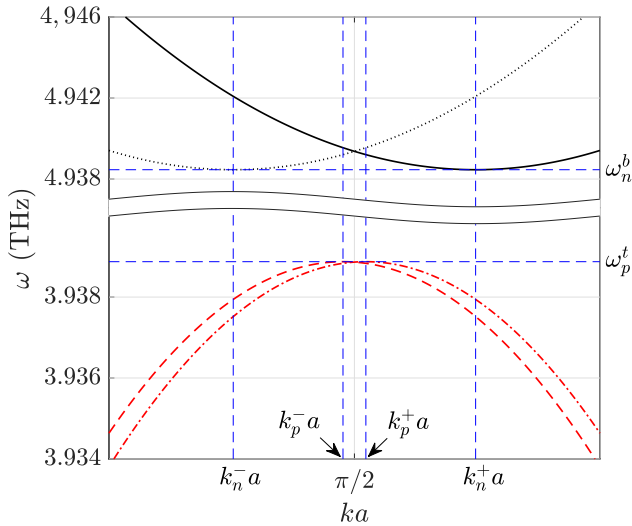


FIG. 4. (color online). Enlarged view of Figs. 3(a) around $k = \pi/(2a)$.

dispersion are expressed as

$$\omega_{n(p)}^{b(t)} = \sqrt{\tilde{\omega}_E} \frac{\sqrt{\omega_E + 2\eta\zeta_+ (2\omega_E + \xi_-) \pm \sqrt{\omega_E}}}{\eta\zeta_+}, \quad (44)$$

where the upper and lower signs of \pm before the square correspond to ω_n^b and ω_p^t respectively, and $\tilde{\omega}_E$, ζ_+ and ξ_- are defined below Eq. (36). From Eq. (44), we get the gap between nutational and precessional bands,

$$\begin{aligned} \Delta_{n-p} &= \frac{1}{\eta} \frac{2\sqrt{\omega_E} (\omega_E^2 + \omega_D^2)^{\frac{1}{4}}}{\sqrt{\omega_E^2 + \omega_D^2} + \omega_E}, \\ &= \frac{1}{\eta} \left[1 - \frac{1}{32} \frac{\omega_D^4}{\omega_E^4} + O\left(\frac{\omega_D^6}{\omega_E^6}\right) \right]. \end{aligned} \quad (45)$$

For the case that $\omega_D \ll \omega_E$, the gap is about $1/\eta$. It should be noted that, for $\eta < \eta_c$, the nutational branches exhibit no extrema at $k = \pm k_n^\pm$, as seen in Fig. 3(c).

3. Chirality and polarization

We now turn to the chirality and polarization, both characterized by a single physical quantity: the ellipticity angle χ defined in Eq. (17). Here, we find that the two sublattices have the same ellipticity angle, i.e. $\chi_n^\pm = -X_n^\pm$ and $\chi_p^\pm = X_p^\pm$, where

$$X_{n,p}^\pm = \frac{1}{2} \arcsin \left(\frac{2\rho_{n,p}^\pm \omega_{n,p}^\pm}{1 + \rho_{n,p}^\pm \omega_{n,p}^\pm} \right). \quad (46)$$

The wave number dependence of χ for nutational and precessional modes is presented in Figs. 3(b) and 3(d).

In contrast to SWs in conventional AFM configurations, the nutational modes here satisfy $\chi_n^\pm < 0$, while the precessional modes are characterized by $\chi_p^\pm > 0$.

This indicates that all nutational branches exhibit left-handed chirality, whereas all precessional branches are right-handed, as also summarized in Tab. III. Another observation is that the chirality is the same for the positive- and negative-frequency branches, as summarized in Tab. III. This result indicates that the chirality depends not only on the sign of frequency, but also on the phase difference between two components of spin-wave fluctuation. It can be inferred from Tab. III that the phase difference ($\delta_\phi - \delta_\theta$) is opposite for the positive- and negative-frequency branches. Thus, according to the definition of ellipticity angle in Eq. (17), χ is unchanged when flipping the sign of frequency. Finally, because the phase difference is identical for two sublattices, i.e. $\delta_{\phi,2j+1} - \delta_{\theta,2j+1} = \delta_{\phi,2j} - \delta_{\theta,2j}$, the chirality is the same for two sublattices, as seen by comparing χ_{2j} and χ_{2j+1} in Tab. III.

Polarization exhibits a strong dependence on the wave number. For the precessional ω_p^- branch, shown by the dashed curves in Figs. 3(b) and 3(d), one finds $\chi_p^- = 0$ at $k = 0$, corresponding to linear polarization. As k increases, χ rises continuously, indicating that the mode evolves from elliptical polarization toward circular polarization. When k reaches k_p^- , the ellipticity angle becomes

$$\begin{aligned} \chi_p^-(k = k_p^-) &= \frac{1}{2} \arcsin \left[\frac{2\sqrt{\omega_E} (\omega_E^2 + \omega_D^2)^{\frac{1}{4}}}{\sqrt{\omega_E^2 + \omega_D^2} + \omega_E} \right] \\ &= \frac{\pi}{4} - \frac{\omega_D^2}{8\omega_E^2} + O\left(\frac{\omega_D^4}{\omega_E^4}\right). \end{aligned} \quad (47)$$

Given the condition $\omega_D \ll \omega_E$, χ_p^- at $k = k_p^-$ is very close to $\pi/4$ and the corresponding mode is nearly circularly polarized. For the precessional ω_p^+ branch, the polarization behavior follows a similar trend, with the only difference being $\chi_p^+ \neq 0$ at $k = 0$. With k increasing from 0, χ_p^+ rises gradually and eventually approaches $\pi/4$ at $k = k_p^+$. The two branches share the same maximum ellipticity angle, i.e. $\chi_p^+(k = k_p^+) = \chi_p^-(k = k_p^-)$.

For nutational SWs, $|\chi_n^\pm|$ attains its minimum at $k = 0$ and its maximum at $k = k_n^\pm$, satisfying $\chi_n^+(k = k_n^+) = \chi_n^-(k = k_n^-) = -\chi_p^-(k = k_p^-)$. Furthermore, the χ - k curves of the two nutational branches are very close to each other and hardly distinguishable, as displayed by the solid and dotted curves in Figs. 3(b) and 3(d). For both nutational branches, the ellipticity (defined by $|\chi_n^\pm|$) increases monotonically with k increasing from 0 and approaches $\pi/4$ at $k = k_n^+$ and $k = k_n^-$ respectively. In summary, precessional SWs exhibit nearly linear polarization in the long-wavelength limit. Near the boundary of Brillouin zone [$k = \pm\pi/(2a)$], both precessional and nutational SWs approach nearly circular polarization.

V. INERTIAL SPIN WAVES IN AFM WITH HOMOGENEOUS DMI

A. Spin waves on top of AFM configuration

Compared with Sec. IV A, the AFM configuration remains identical, while the DMI term is modified into the staggered form. Following the same procedure as in Sec. IV A, with details provided in Appendix D, the components of the spin-wave fluctuations can again be expressed in the form of Eqs. (22) and (23). The degeneracy is lifted under homogeneous DMI. Eight spin-wave branches are obtained, four with positive frequencies and four with negative frequencies. Their amplitudes and initial phases, as well as the ellipticity angles [calculated from Eq. (17)] are listed in Tab. IV for every branches of SWs. To better clarify these characteristics, we illustrate the precessional trajectories of the magnetization tip for all modes of the two sublattices in Tab. V. This schematic clearly presents their chirality, amplitude ratios and phase differences. Additionally, we plot the dispersions and the dependence of sublattice amplitude ratios on the wave number in Fig. 5 in the whole Brillouin zone.

In Tab. IV, the eigenfrequencies of nutational and precessional SWs read

$$\omega_{n,p}^{\pm} = \frac{\sqrt{1 + \eta\Gamma \pm \sqrt{(1 + \eta\Gamma)^2 - \eta^2\Lambda_{\pm}^2}}}{\sqrt{2}\eta}, \quad (48)$$

where $\Gamma = 4\sqrt{\omega_E^2 + \omega_D^2}$, and $\Lambda_{\pm} = 4[(\omega_E^2 + \omega_D^2) - (\omega_E^2 + \omega_D^2)\cos^2(ka \mp \varphi_d)]^{1/2}$, with ω_D^c defined in Eq. (19), and $\varphi_d = \tan^{-1}(\omega_E, \omega_D)$. In Eq. (48), the upper and lower signs in front of the square root correspond to the n and p branches, respectively. Similar to Sec. IV A, Λ_{\pm} is purely imaginary for some values of k when $\omega_D > \omega_D^c$, yielding $\Lambda_{\pm}^2 < 0$. Consequently, $\omega_{n,p}^{\pm}$ becomes complex according to Eq. (48), indicating the instability of AFM configuration. Here, the degeneracy is lifted by the DMI. When $\omega_D = 0$, one has $\varphi_d = 0$, which further leads to $\omega_{n,p}^+ = \omega_{n,p}^-$, signifying the recovery of degeneracy for both nutational and precessional SWs.

In Tab. IV, the parameters $\rho_{n,p}^{\pm}$ are given by

$$\rho_{n,p}^{\pm} = \pm \frac{2\sqrt{\omega_E^2 + \omega_D^2} \cos(ka \mp \varphi_d)}{\eta\omega_{n,p}^{\pm 2} \pm \omega_{n,p}^{\pm} - 2\sqrt{\omega_E^2 + \omega_D^2}}. \quad (49)$$

Here, the leading \pm sign and the \mp sign in front of $\omega_{n,p}^{\pm}$ are associated with the subscripts n and p , respectively, whereas the \mp sign in the argument of the cosine is associated with the superscript \pm of $\rho_{n,p}^{\pm}$. It can be verified that $\eta\omega_{n,p}^{\pm 2} + \omega_{n,p}^{\pm} - 2\sqrt{\omega_E^2 + \omega_D^2} > 0$ and $-(\eta\omega_{n,p}^{\pm 2} - \omega_{n,p}^{\pm} - 2\sqrt{\omega_E^2 + \omega_D^2}) > 0$. So, the signs of $\rho_{n,p}^{\pm}$ are determined by $\cos(ka \mp \varphi_d)$.

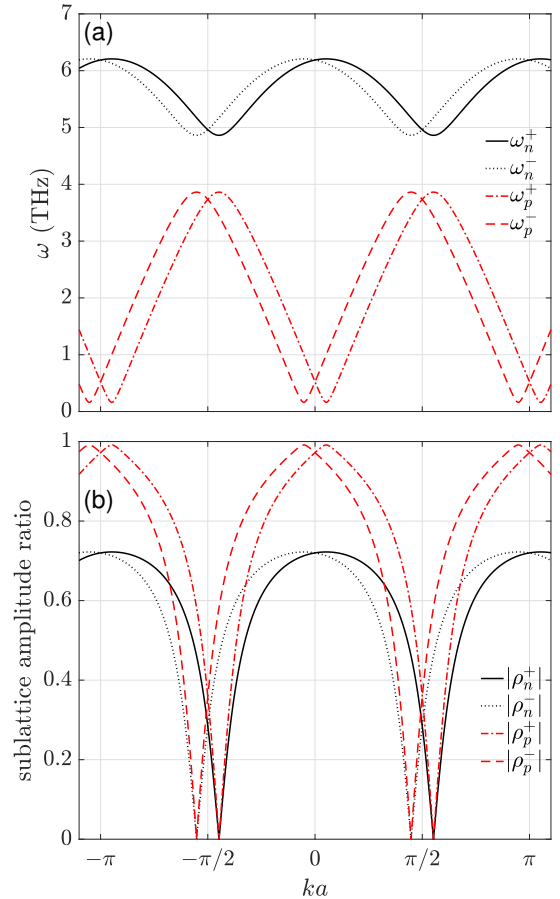


FIG. 5. (color online). Dispersion (a) and sublattice amplitude ratio (b) of the SWs on top of an AFM configuration for the case of homogeneous DMI. Here, all parameters remain identical to those in Fig. 2.

1. Dispersion

In Fig. 5(a), the overall spin-wave spectrum exhibits no nonreciprocity. Nevertheless, individual spin-wave modes are nonreciprocal and emerge in pairs with opposite chirality. Their dispersion curves shift in opposite directions, while the combined spectrum remains reciprocal.

In contrast to Sec. IV A, which investigates SWs in the AFM configuration with staggered DMI, homogeneous DMI breaks the spin-wave degeneracy by shifting the dispersions along k axis by $\pm\varphi_d/a$. This feature can be clearly observed by comparing Fig. 5(a) and 2(a). This distinction originates from their symmetry-breaking properties: homogeneous DMI breaks parity combined with time-reversal (\mathcal{PT}) symmetry, whereas staggered DMI preserves it. Under spatial inversion, which is equivalent to interchanging the two magnetic sublattices, the homogeneous DMI term flips its sign and thereby breaks the \mathcal{PT} symmetry of uniaxial antiferromagnets. By contrast, the staggered DMI term remains invariant under

TABLE IV. Amplitudes, phases, and ellipticity angles of the SWs on top of an AFM configuration for homogeneous DMI. Here, $H(\lambda^\pm)$ is the unit step function and $\lambda^\pm = \text{sgn}[\cos(ka \mp \varphi_d)]$.

	ω_n^+	$-\omega_n^+$	ω_n^-	$-\omega_n^-$	ω_p^+	$-\omega_p^+$	ω_p^-	$-\omega_p^-$
$A_{\theta,2j}$	$\frac{ \rho_n^+ }{\omega_n^+}$	$\frac{1}{\omega_n^+}$	$\frac{1}{\omega_n^-}$	$\frac{ \rho_n^- }{\omega_n^-}$	$\frac{ \rho_p^+ }{\omega_p^+}$	$\frac{1}{\omega_p^+}$	$\frac{1}{\omega_p^-}$	$\frac{ \rho_p^- }{\omega_p^-}$
$A_{\phi,2j}$	$\frac{ \rho_n^+ }{\omega_n^+}$	$\frac{1}{\omega_n^+}$	$\frac{1}{\omega_n^-}$	$\frac{ \rho_n^- }{\omega_n^-}$	$\frac{ \rho_p^+ }{\omega_p^+}$	$\frac{1}{\omega_p^+}$	$\frac{1}{\omega_p^-}$	$\frac{ \rho_p^- }{\omega_p^-}$
$\delta_{\theta,2j}$	$\pi H(-\lambda^+)$	$\pi H(\lambda^+)$	$\pi H(\lambda^-)$	$\pi H(-\lambda^-)$	$\pi H(\lambda^+)$	$\pi H(-\lambda^+)$	$\pi H(-\lambda^-)$	$\pi H(\lambda^-)$
$\delta_{\phi,2j}$	$\lambda^+ \frac{\pi}{2}$	$-\lambda^+ \frac{\pi}{2}$	$\lambda^- \frac{\pi}{2}$	$-\lambda^- \frac{\pi}{2}$	$-\lambda^+ \frac{\pi}{2}$	$\lambda^+ \frac{\pi}{2}$	$-\lambda^- \frac{\pi}{2}$	$\lambda^- \frac{\pi}{2}$
$A_{\theta,2j+1}$	$\frac{1}{\omega_n^+}$	$\frac{ \rho_n^+ }{\omega_n^+}$	$\frac{ \rho_n^- }{\omega_n^-}$	$\frac{1}{\omega_n^-}$	$\frac{1}{\omega_p^+}$	$\frac{ \rho_p^+ }{\omega_p^+}$	$\frac{ \rho_p^- }{\omega_p^-}$	$\frac{1}{\omega_p^-}$
$A_{\phi,2j+1}$	$\frac{1}{\omega_n^+}$	$\frac{ \rho_n^+ }{\omega_n^+}$	$\frac{ \rho_n^- }{\omega_n^-}$	$\frac{1}{\omega_n^-}$	$\frac{1}{\omega_p^+}$	$\frac{ \rho_p^+ }{\omega_p^+}$	$\frac{ \rho_p^- }{\omega_p^-}$	$\frac{1}{\omega_p^-}$
$\delta_{\theta,2j+1}$	0	π	π	0	0	π	π	0
$\delta_{\phi,2j+1}$	$-\frac{\pi}{2}$	$\frac{\pi}{2}$	$-\frac{\pi}{2}$	$\frac{\pi}{2}$	$-\frac{\pi}{2}$	$\frac{\pi}{2}$	$-\frac{\pi}{2}$	$\frac{\pi}{2}$
χ_{2j}	$\frac{\pi}{4}$	$-\frac{\pi}{4}$	$-\frac{\pi}{4}$	$\frac{\pi}{4}$	$\frac{\pi}{4}$	$-\frac{\pi}{4}$	$-\frac{\pi}{4}$	$\frac{\pi}{4}$
χ_{2j+1}	$-\frac{\pi}{4}$	$\frac{\pi}{4}$	$\frac{\pi}{4}$	$-\frac{\pi}{4}$	$-\frac{\pi}{4}$	$\frac{\pi}{4}$	$\frac{\pi}{4}$	$-\frac{\pi}{4}$

TABLE V. Schematic diagrams of the SWs on top of an AFM configuration for the case of homogeneous DMI. The blue solid (red dotted) circles denote the trajectories of the tips of \mathbf{m}_{2j} (\mathbf{m}_{2j+1}). The arrows on the blue solid (red dotted) circles signify the rotational senses of \mathbf{m}_{2j} (\mathbf{m}_{2j+1}) around $-\mathbf{r}_r^{2j}$ (\mathbf{e}_r^{2j+1}). The blue solid (red dotted) vectors line represent the fluctuation $\delta\mathbf{m}_{2j}$ ($\delta\mathbf{m}_{2j+1}$).

	ω_n^+	$-\omega_n^+$	ω_n^-	$-\omega_n^-$	ω_p^+	$-\omega_p^+$	ω_p^-	$-\omega_p^-$
$\lambda_\pm > 0$								
$\lambda_\pm < 0$								
$\lambda_+ > 0$ $\lambda_- < 0$								
$\lambda_+ < 0$ $\lambda_- > 0$								
frame								

this operation.

Near the top of nutational dispersion and the bottom of precessional one ($k = \pm\varphi_d/a$), the frequencies expanded to second order in $k \pm \varphi_d/a$ read

$$\omega_{n,p}^\pm = \sqrt{\Delta_{n,p}^2 \pm v^2 (k \mp \varphi_d/a)^2}, \quad (50)$$

with the sign \mp in front of φ_d/a corresponding to the

superscript \pm of $\omega_{n,p}^\pm$, and the sign \pm before v^2 corresponding to the subscript (n,p) of $\omega_{n,p}^\pm$. The frequency at the top of nutational dispersion Δ_n and the gap of the precessional dispersion Δ_p are given by Eq. (27). The characteristic velocity v is given by Eq. (29).

The nutational ω_n^+ and ω_n^- branches reach their band minima at $k = (\pm\pi/2 + \varphi_d)/a$ and $k = (\pm\pi/2 - \varphi_d)/a$, respectively, while the corresponding precessional branches

ω_p^+ and ω_p^- reach their band maxima at the same wave numbers. The frequencies at the bottom of nutational band and the top of precessional band are still Eq. (30).

As $\eta \rightarrow 0$, ω_n^\pm diverges and vanishes. The dispersion displayed in Fig. 5(a) is consistent with the result reported in Ref. [65].

2. Sublattice amplitude ratio

The amplitude ratio of SWs between two sublattices can be represented by $|\rho_{n,p}^\pm|$, which varies with k , as displayed in Fig. 5(b). The sublattice amplitude ratios of the ω_n^+ - and ω_p^+ -branches reach their maxima at $k = \varphi_d/a$, whereas those of the ω_n^- - and ω_p^- -branches reach their maxima at $k = -\varphi_d/a$. In particular, the ratio is close to 1 for the precessional mode. In the limit $\omega_K \ll \omega_E$ and $\omega_D \ll \omega_E$, ρ_p^\pm reduces to the expression given in Eq. (31). Owing to the relative smallness of ω_K and ω_D , ρ_p^0 is about 1 and the angle φ_d is small. From this, we can conclude that the amplitudes of two sublattices are closest to each other near the long-wavelength limit. With increasing k from $k = 0$, $|\rho_{n,p}^\pm|$ decreases gradually. The amplitude ratio $\rho_{n,p}^+$ vanishes at $k = (\pm\pi/2 + \varphi_d)/a$, while $\rho_{n,p}^-$ vanishes at $k = (\pm\pi/2 - \varphi_d)/a$. This implies that only a single sublattice can be excited for short-wavelength SWs with $\lambda \approx 4a$. In addition, it is worth mentioning that the amplitude ratios corresponding to positive- and negative-frequency branches are mutually reciprocal, as is evident by comparing the A_θ and A_ϕ data listed in Tab. IV. This feature is also illustrated schematically in Tab. V.

3. Chirality and phase

Since we adopt local coordinate frames (shown in Tab. V) throughout spin-wave calculations, chirality is defined as the rotational sense about the static magnetization of each individual sublattice. Following this definition, SWs of two sublattices exhibit opposite signs of χ with $|\chi| = \pi/4$, indicating opposite chiralities that correspond to lefthanded and righthanded circular polarizations.

It is generally acknowledged that the nutational SWs are lefthanded and the precessional SWs are righthanded. Here, we find that one branch nutational SW exhibits lefthanded polarization, whereas the other branch is righthanded, and the same behavior applies to precessional SWs. Additionally, flipping the sign of eigenfrequency can reverse the chirality of SWs. As listed in Tab. IV, the phase difference ($\delta_{\phi,l} - \delta_{\theta,l}$) of two components of $\delta\mathbf{m}_l$ remains unchanged under the sign reversal of ω . Therefore, according to the definition of ellipticity angle in Eq. (17), the sign of χ is the identical to that of ω .

In Tab. V, we schematically illustrate the phases of all modes at a specific lattice site at a given instant in time. It reveals that the phase relation between the oscillations of two sublattices depends on the wave number.

More specifically, for $0 < |k|a < \pi/2 - \varphi_d$ ($\lambda_\pm > 0$), the two sublattices oscillate in phase for nutation and in antiphase for precession; for $\pi/2 + \varphi_d < |k|a < \pi$ ($\lambda_\pm < 0$), the phase relations are reversed. In the narrow region $\pi/2 - \varphi_d < ka < \pi/2 + \varphi_d$ ($\lambda_+ > 0$ and $\lambda_- < 0$), the two sublattices oscillate in phase for the ω_n^+ and ω_p^- modes and in antiphase for the ω_n^- and ω_p^+ modes. The phase behavior is reversed in the interval $-\pi/2 - \varphi_d < ka < -\pi/2 + \varphi_d$ (where $\lambda_+ < 0$ and $\lambda_- > 0$).

B. Spin waves on top of spiral configuration

When $\omega_D > \omega_D^c$, the static configuration is spiral with a helical angle ϕ_s [Eq. (20)], as schematically displayed in Fig. 1(b). Applying the method presented in Sec. II, the spin-wave modes obtained in Appendix E can be expressed in the form of Eq. (16). The spin-wave spectrum consists of four branches: two positive-frequency branches and their two negative-frequency counterparts. Their amplitudes, initial phases, and ellipticity angles are listed in Tab. VI for all spin-wave branches.

The above results reveal that SWs based on the spiral configuration correspond exactly to the low-frequency branch of nutational and precessional SWs in the canted magnetic configuration. Accordingly, their dispersion relations, oscillation amplitudes, phase characteristics and ellipticity angles are identical to those of the $\omega_{n,p}^-$ spin-wave branches within the canted configuration, which is verified by a comparison between Table VI and the data of $\omega_{n,p}^-$ branches listed in Tab. III.

This correspondence is not a coincidence: it originates from the invariance of dispersion relations under local unitary transformations [66]. Transforming the magnetic energy with a homogeneous DMI [Eq. (18)] into the local frame defined by Eq. (2) for the spiral state yields

$$E_{\text{spiral}} = \sum_l \left[\sqrt{\omega_E^2 + \omega_D^2} \left(m_l^r m_{l+1}^r + m_l^\phi m_{l+1}^\phi \right) + \omega_E m_l^\theta m_{l+1}^\theta - \omega_K (m_l^\theta)^2 \right], \quad (51)$$

which corresponds to a FM spin chain with anisotropic exchange and uniaxial magnetic anisotropy, and gives the spin-wave dispersions of spiral configuration. In the local frame defined by Eq. (2) and the canted state, the magnetic energy with a staggered DMI [Eq. (18)] differs from E_{spiral} only by an extra minus sign in the first term. By further rotating \mathbf{m}_l by π around the local \mathbf{e}_θ^l axis, we attain $E_{\text{canted}} = E_{\text{spiral}}$, which ensures that the spin-wave dispersion of the canted configuration (its ω_n^- - and ω_p^- -branches) is identical to that of the spiral configuration.

To understand the emergence of $\omega_{n,p}^+$ spin-wave branch on the canted configuration, one can invoke band folding [67]. The equivalent ferromagnetic chain described by Eq. (51) supports the $\omega_{n,p}^-$ dispersion defined in the extended Brillouin zone $k \in [-\pi/a, \pi/a]$. In contrast, the original canted configuration has two magnetic atoms per primitive cell, so its first Brillouin zone is

TABLE VI. Amplitudes, phases, and ellipticity angles of the SWs on top of a spiral configuration for homogeneous DMI. Here, $X_{n,p} = \frac{1}{2} \arcsin\left(\frac{2\rho_{n,p}\omega_{n,p}}{1+\rho_{n,p}^2\omega_{n,p}^2}\right)$.

	ω_n	$-\omega_n$	ω_p	$-\omega_p$
$\rho_{\theta,l}$	ρ_n	ρ_n	ρ_p	ρ_p
$\rho_{\phi,l}$	$\frac{1}{\omega_n}$	$\frac{1}{\omega_n}$	$\frac{1}{\omega_p}$	$\frac{1}{\omega_p}$
$\delta_{\theta,l}$	π	π	0	0
$\delta_{\phi,l}$	$\frac{\pi}{2}$	$-\frac{\pi}{2}$	$\frac{\pi}{2}$	$-\frac{\pi}{2}$
χ_l	$-X_n$	$-X_n$	X_p	X_p

reduced to $k \in [-\pi/(2a), \pi/(2a)]$. By folding the $\omega_{n,p}^-$ dispersion from the outer intervals $[-\pi/a, -\pi/(2a)]$ and $[\pi/(2a), \pi/a]$ into this reduced zone, one obtain the $\omega_{n,p}^+$ branch. Specifically, the dispersions in $[-\pi/a, -\pi/(2a)]$ is translated by π/a , and that in $[\pi/(2a), \pi/a]$ by $-\pi/a$. This yields $\omega_{n,p}^+(k) = \omega_{n,p}^-(k \pm \pi/a)$, a relation that can also be verified using Eq. (32).

VI. DISCUSSIONS

We first compare the spin-wave degeneracies in the AFM configuration under homogeneous and staggered DMIs. The degeneracy is lifted in the presence of homogeneous DMI but preserved under staggered DMI, which originates from the intrinsic symmetry difference between the two DMI forms. It is well established that \mathcal{PT} symmetry guarantees the double degeneracy of SWs in uniaxial AFM systems. For homogeneous DMI, interchanging the two magnetic sublattices flips the sign of the DMI term, which breaks \mathcal{P} symmetry, and further destroys the overall \mathcal{PT} -symmetry. Consequently, the two originally degenerate spin-wave dispersions shift oppositely along the k -axis, as illustrated in Fig. 5(a). By contrast, staggered DMI retains intact \mathcal{PT} symmetry, such that the spin-wave degeneracy remains unaltered, as depicted in Fig. 2(a).

Following the same symmetry-based reasoning, we compare the dispersions of SWs atop the collinear AFM and canted configurations, as shown in Figs. 2(a) and 3(a). In the AFM configuration, the system preserves the \mathcal{PT} symmetry. Combining with the \mathcal{PT} symmetric staggered DMI, the spin-wave degeneracy is not lifted. In contrast, the canted configuration breaks both \mathcal{P} and the \mathcal{T} symmetries, even though the staggered DMI itself remains \mathcal{PT} symmetric. As a result, the originally twofold degenerate spin-wave spectrum is completely lifted: near the zone center ($k = 0$) the two branches split along the ω -axis, much like the separation into an acoustic (gapless) and an optical (gapped) branch; near the zone boundary [$k = \pm\pi/(2a)$] they shift along the k -axis. The former splitting arises directly from the \mathcal{T} symmetry breaking. The latter shifting originates from the \mathcal{P} symmetry breaking. In the presence of \mathcal{P} symmetry, the

dispersion must satisfy $\omega(k_b + \delta k) = \omega(k_b - \delta k)$ with $k_b = \pi/(2a)$, which forces the group velocity at the zone boundary to vanish and pins the extrema at this high-symmetry point. Once the \mathcal{P} symmetry is broken, the group velocities at the zone boundary become nonzero and opposite in sign for the two branches; consequently, their extrema are no longer pinned at the high-symmetry point but shift in opposite directions, leading to a crossing and an apparent lateral displacement, as shown in Fig. 4.

After the degeneracy is lifted, each dispersion branch remains an even function of k . This can be understood from a symmetry perspective: although \mathcal{T} and \mathcal{P} are individually broken, the canted state still preserves the anti-unitary symmetry that combines time reversal with a π rotation about the z axis, $\mathcal{TR}_z(\pi)$. Under this operation, each magnon branch is mapped onto itself at the opposite k , which enforces $\omega(k) = \omega(-k)$ for every branch.

Second, there exists a prevalent yet misleading notion that reversing the sign of frequency will invert the chirality of SWs. This conclusion holds true only for several simple spin-wave forms, such as the spin fluctuation $\delta\mathbf{m} = \delta m_x \cos\omega t \mathbf{e}_x + \delta m_y \sin\omega t \mathbf{e}_y$. Upon replacing ω with $-\omega$, the chirality of $\delta\mathbf{m}$ switches from right-handed to left-handed. However, the general solutions, as exemplified in Eq. (16), are not that straightforward. The initial phases of each component in the spin-wave solutions, and consequently the phase differences between these components, generally differ between positive-frequency and negative-frequency solutions, as illustrated in Tabs. I, III, IV, and VI. Therefore, it is essential to adhere to the general principle that the chirality of the superposition of two perpendicular harmonic oscillations depends on their phase difference. The ellipticity angle χ defined in Eq. (17) takes into account both the phase difference between spin-wave components and the sign of frequency. The sign of χ characterizes the spin-wave chirality, while its magnitude denotes the polarization ellipticity. This definition covers all polarization states including linear, elliptical and circular polarizations, as well as all possible orientations of the trajectory traced by the magnetization vector tip. In the discussed cases, flipping the frequency sign exerts no influence on the chirality of SWs in spiral, canted and staggered-DMI AFM configurations. By contrast, such an operation reverses the chirality of SWs in homogeneous-DMI AFM configuration.

We note that, building upon the lengths of the principal axes of the elliptical precession trajectory, Ref. [64] recently proposed a signed ellipticity parameter to quantify the polarization and chirality of SWs. However, this definition only captures axis-aligned elliptical polarization states (with principal axes aligned with the coordinate axes) and linear polarization along the x -axis, failing to describe elliptical and linear polarizations with arbitrary orientations—i.e., all possible polarization states.

Third, we adopt the classical linearization approach to derive spin-wave solutions. By solving the eigenvalues

and eigenvectors of the linearized dynamic equations, explicit analytical expressions for SWs can be directly acquired from the corresponding eigenvectors. In this way, the key spin-wave characteristics, including dispersion relations, amplitudes, phases, chiralities, and polarization states, can be readily extracted from the eigenvalues and eigenvectors. The proposed method therefore provides a general and efficient framework for characterizing inertial spin waves. The quantum formalism, based on the Holstein-Primakoff transformation, Fourier transformation, and Bogoliubov transformation, offers a powerful and systematic description of magnonic excitations. However, when the goal is to obtain explicit spin-wave amplitudes, phases, chiralities, and polarization states, these quantities may be less transparent in the Bogoliubov representation and require additional reconstruction. In this respect, the classical linearization approach provides a more direct route to chirality and polarization, while remaining fully complementary to the quantum approach. The latter is particularly advantageous for addressing intrinsically quantum phenomena, such as magnon-magnon interactions, nonlinear effects, magnon Bose-Einstein condensation, and related many-body processes.

Fourth, most nutation SWs [as shown in Figs. 2(a), 3(a) and 5(a)] exhibit backward propagation characteristics (i.e., group velocity antiparallel to the wavevector) in the long-wavelength regime. This differs from classical backward volume magnetostatic SWs [68], which originate from magnetostatic dipole interactions. A similar backward feature was also reported for dipolar-governed nutation SWs in thin films [45]. Such conventional SWs show backward behavior only along specific propagation directions (e.g., near the in-plane magnetic field or in coupled layer structures) and within the gigahertz frequency range. For nutation SWs governed by the inertial LLG equation, however, the backward characteristic is nearly universal: the group velocity is oriented opposite to the wavevector for almost all propagation directions. Inertial nutation SWs therefore constitute a distinct category of backward SWs. They support backward energy transport without specially designed magnetostatic boundary conditions and open new opportunities for developing ultrafast terahertz spin-wave devices.

Finally, nonreciprocal effects in chiral magnets have previously been reported to emerge only at small wave numbers near the Brillouin zone center. By contrast, Figs. 3(a), 3(c), 4 and 5(a) reveal nonreciprocity extending to the Brillouin zone boundary.

VII. CONCLUSIONS

In this work, we propose a straightforward scheme for calculating inertial SWs in both uniform and nonuniform magnetic structures. After linearizing the inertial Landau-Lifshitz equation and recasting it into a set of first-order differential equations, we adopt standard linear-algebra techniques to directly solve for all eigen-

values and eigenvectors of inertial SWs. The corresponding amplitudes, dispersion relations, phases, chirality and polarizations can then be readily obtained. We apply this method to uniaxial AFMs with staggered and homogeneous DMIs, where uniform AFM, canted and spiral configurations emerge depending on the magnitude of DMI. Around these equilibrium magnetic configurations, we derive compact formulae for the dispersion relation, the sublattice amplitude ratio and the ellipticity angle (which jointly define chirality and polarization).

Detailed analysis of the calculated results uncovers key characteristics of inertial SWs in several magnetic configurations, as follows: (1) weak staggered DMI fails to lift the degeneracy of both nutational and precessional SWs, whereas weak homogeneous DMI does so. Under strong DMIs, the magnetic configurations are nonuniform and the SWs are fully non-degenerate. (2) In the long-wavelength regime, nutational SWs are generally backward waves with negative group velocities. For canted and spiral configurations, the group velocity of one nutational branch flips sign at a certain inertial relaxation time (η), producing flat bands. Our calculations show that under identical DMI strength, nutational and precessional SWs in spiral configuration coincide with the low-frequency branches of their counterparts in canted configuration. Band folding and dispersion-preserving unitary transformations naturally account for this equivalence. (3) The sublattice amplitude ratio of uniform AFM configurations strongly depends on the wave number and spin-wave branch, while SWs in canted configuration possess identical sublattice amplitude and polarization. (4) In the uniform AFM configurations, circularly polarized SWs with opposite chiralities always emerge in pairs, regardless of whether they are nutational or precessional SWs. For canted and spiral configurations, nutational SWs are always left-handed, while precessional SWs are always right-handed. (5) Spin wave polarization is insensitive to wave number for uniform AFM configurations, but strongly dependent on wave number for canted and spiral configurations.

The proposed methodology can be generalized to investigate inertial SWs in a broad range of magnetic configurations. Moreover, our findings provide a comprehensive characterization of inertial SWs in uniaxial DMI AFMs, which not only enriches the fundamental understanding of magnetic inertial effects but also offers valuable insights for the applied research of ultrafast magnonics.

VIII. ACKNOWLEDGMENTS

This work was supported by the NSF of Changsha City (Grant No. kq2208008), the NSF of Hunan Province (Grant No. 2023JJ30116), the key Program of Education Bureau of Hunan Province (Grant No.24A0494) and the Regional Joint Funds of the NSF of Hunan Province (Grant No.2024JJ7312).

Appendix A: Expansion of effective field

In this section, we give the linear expansion of Eq. (5). Inserting the spin-wave ansatz expressed by Eqs. (3) and (4), the magnetic energy can be written as a quadratic function of $m_{\theta,l}$ and $m_{\phi,l}$. The zeroth-order contribution to the effective field is then given by

$$\mathbf{h}_l^0 = - \left(\frac{\partial E}{\partial m_{\theta,l}} \right)_0 \mathbf{e}_{\theta}^l - \left(\frac{\partial E}{\partial m_{\phi,l}} \right)_0 \mathbf{e}_{\phi}^l, \quad (\text{A1})$$

$$\begin{aligned} \delta \mathbf{h}_l = & - \left\{ \left[\left(\frac{\partial^2 E}{\partial m_{\theta,l}^2} \right)_0 m_{\theta,l} + \left(\frac{\partial^2 E}{\partial m_{\theta,l} \partial m_{\phi,l}} \right)_0 m_{\phi,l} \right] + \left[\left(\frac{\partial^2 E}{\partial m_{\theta,l} \partial m_{\theta,l+1}} \right)_0 m_{\theta,l+1} + \left(\frac{\partial^2 E}{\partial m_{\theta,l} \partial m_{\phi,l+1}} \right)_0 m_{\phi,l+1} \right] \right. \\ & + \left. \left[\left(\frac{\partial^2 E}{\partial m_{\theta,l} \partial m_{\theta,l-1}} \right)_0 m_{\theta,l-1} + \left(\frac{\partial^2 E}{\partial m_{\theta,l} \partial m_{\phi,l-1}} \right)_0 m_{\phi,l-1} \right] \right\} \mathbf{e}_{\theta}^l \\ & - \left\{ \left[\left(\frac{\partial^2 E}{\partial m_{\phi,l}^2} \right)_0 m_{\phi,l} + \left(\frac{\partial^2 E}{\partial m_{\phi,l} \partial m_{\theta,l}} \right)_0 m_{\theta,l} \right] + \left[\left(\frac{\partial^2 E}{\partial m_{\phi,l} \partial m_{\phi,l+1}} \right)_0 m_{\phi,l+1} + \left(\frac{\partial^2 E}{\partial m_{\phi,l} \partial m_{\theta,l+1}} \right)_0 m_{\theta,l+1} \right] \right. \\ & + \left. \left[\left(\frac{\partial^2 E}{\partial m_{\phi,l} \partial m_{\phi,l-1}} \right)_0 m_{\phi,l-1} + \left(\frac{\partial^2 E}{\partial m_{\phi,l} \partial m_{\theta,l-1}} \right)_0 m_{\theta,l-1} \right] \right\} \mathbf{e}_{\phi}^l. \end{aligned} \quad (\text{A2})$$

$\delta \mathbf{h}_l$ can be calculated by the derivatives of magnetic energy with respect to the components of SW fluctuation. Eqs. (A1) and (A2) yield the expansion given in Eq. (6).

Appendix B: SW solution in staggered-DMI antiferromagnetic configuration

When $\omega_D < \omega_D^c$, the AFM configuration is preferred, which is double degenerate. Without loss of generality, we chose $\mathbf{m}_{2j}^0 = -\mathbf{e}_z$ and $\mathbf{m}_{2j+1}^0 = \mathbf{e}_z$. In the coordinate system shown in Fig. 1(a), the parametrization given in Eq. (2) becomes singular when \mathbf{m}_l^0 is aligned with the z axis, since ϕ_l^0 is ill-defined. To resolve this singularity, we instead employ a rotated frame in which $\mathbf{m}_{2j}^0 = -\mathbf{e}_x$ and $\mathbf{m}_{2j+1}^0 = \mathbf{e}_x$, corresponding to $\theta_{2j}^0 = \theta_{2j+1}^0 = \pi/2$, $\phi_{2j}^0 = \pi$ and $\phi_{2j+1}^0 = 0$. Then we combine this equilibrium magnetization with the spin-wave fluctuations in Eq. (4) to obtain the total magnetization. Substituting the resultant expression into the reduced magnetic energy in Eq. (18) for staggered DMI (where \mathbf{e}_z is replaced by \mathbf{e}_x), along with the coordinate transformation given in Eq. (2), one can explicitly calculate all matrices in Eq. (9) as follows: $\mathcal{H}_l = 2 \text{diag}[\omega_E + \omega_K, \omega_E + \omega_K]$, and

$$\mathcal{H}_{l\pm 1} = \begin{pmatrix} \omega_E & -(-1)^l \omega_D \cos \phi_l^0 \\ -(-1)^l \omega_D \cos \phi_l^0 & -\omega_E \end{pmatrix}. \quad (\text{B1})$$

Next, the parameter matrixes \mathcal{M}_l and $\mathcal{M}_{l\pm 1}$ in Eq. (15) can be assembled using Eqs. (8), (12) and (13). Since $\mathcal{H}_{l\pm 1}$ depends on ϕ_l^0 ($\phi_{2j}^0 = \pi$ and $\phi_{2j+1}^0 = 0$), it follows that $\mathcal{H}_{l\pm 1}$ is identical across all lattice sites within each sublattice, while distinct between two differ-

where the subscript '0' denotes evaluation at the equilibrium state. Only considering the nearest-neighbor exchange coupling, the linear-order term of the effective field reads

ent sublattices. Thus, the complex amplitudes in the plane-wave ansatz [Eq. (14)] should be extended as $(\mathcal{A}_{\theta}^e, \mathcal{A}_{\phi}^e, \mathcal{A}_{\theta}^o, \mathcal{A}_{\phi}^o)^T$, with $\mathcal{A}_{\theta}^{e(o)}$ and $\mathcal{A}_{\phi}^{e(o)}$ being the uniform amplitudes of even (odd) sites, and T denoting the transpose of matrix. Then the spin-wave equations [Eq. (15)] for two sublattices can be written as

$$\mathcal{M}_{2j} \begin{pmatrix} \mathcal{A}_{\theta}^e \\ \mathcal{A}_{\phi}^e \\ \omega \mathcal{A}_{\theta}^o \\ \omega \mathcal{A}_{\phi}^o \end{pmatrix} + \widetilde{\mathcal{M}}_{2j} \begin{pmatrix} \mathcal{A}_{\theta}^o \\ \mathcal{A}_{\phi}^o \\ \omega \mathcal{A}_{\theta}^e \\ \omega \mathcal{A}_{\phi}^e \end{pmatrix} = \omega \begin{pmatrix} \mathcal{A}_{\theta}^e \\ \mathcal{A}_{\phi}^e \\ \omega \mathcal{A}_{\theta}^o \\ \omega \mathcal{A}_{\phi}^o \end{pmatrix}, \quad (\text{B2})$$

and

$$\mathcal{M}_{2j+1} \begin{pmatrix} \mathcal{A}_{\theta}^o \\ \mathcal{A}_{\phi}^o \\ \omega \mathcal{A}_{\theta}^e \\ \omega \mathcal{A}_{\phi}^e \end{pmatrix} + \widetilde{\mathcal{M}}_{2j+1} \begin{pmatrix} \mathcal{A}_{\theta}^e \\ \mathcal{A}_{\phi}^e \\ \omega \mathcal{A}_{\theta}^o \\ \omega \mathcal{A}_{\phi}^o \end{pmatrix} = \omega \begin{pmatrix} \mathcal{A}_{\theta}^o \\ \mathcal{A}_{\phi}^o \\ \omega \mathcal{A}_{\theta}^e \\ \omega \mathcal{A}_{\phi}^e \end{pmatrix}, \quad (\text{B3})$$

where $\widetilde{\mathcal{M}}_l = e^{ika} \mathcal{M}_{l+1} + e^{-ika} \mathcal{M}_{l-1}$. Combining these two matrixes equations (B2) and (B3), and calculating the parameter matrixes \mathcal{M}_l and $\mathcal{M}_{l\pm 1}$, we derive the

matrix-form eigen equation for SWs as follows:

$$\mathcal{M} \begin{pmatrix} \mathcal{A}_\theta^e \\ \mathcal{A}_\phi^e \\ \mathcal{A}_\theta^o \\ \mathcal{A}_\phi^o \\ \omega \mathcal{A}_\theta^e \\ \omega \mathcal{A}_\phi^e \\ \omega \mathcal{A}_\theta^o \\ \omega \mathcal{A}_\phi^o \end{pmatrix} = \omega \begin{pmatrix} \mathcal{A}_\theta^e \\ \mathcal{A}_\phi^e \\ \mathcal{A}_\theta^o \\ \mathcal{A}_\phi^o \\ \omega \mathcal{A}_\theta^e \\ \omega \mathcal{A}_\phi^e \\ \omega \mathcal{A}_\theta^o \\ \omega \mathcal{A}_\phi^o \end{pmatrix}, \quad (\text{B4})$$

where the parameter matrix

$$\mathcal{M} = \begin{pmatrix} O_4 & I_4 \\ \mathcal{M}_{21} & \mathcal{M}_{22} \end{pmatrix}, \quad (\text{B5})$$

with O_4 and I_4 being the 4×4 zero matrix and identity matrix, respectively. In Eq. (B5),

$$\mathcal{M}_{22} = \frac{i}{\eta} \begin{pmatrix} 0 & 1 & 0 & 0 \\ -1 & 0 & 0 & 0 \\ 0 & 0 & 0 & -1 \\ 0 & 0 & 1 & 0 \end{pmatrix}, \quad (\text{B6})$$

$$\mathcal{V} = \begin{pmatrix} \frac{\rho_n}{\omega_n} e^{-i\varphi_0} & -\frac{e^{i\varphi_0}}{\rho_n \omega_n} & \frac{\rho_n}{\omega_n} e^{i\varphi_0} & -\frac{e^{-i\varphi_0}}{\rho_n \omega_n} & \frac{\rho_p}{\omega_p} e^{i\varphi_0} & -\frac{e^{-i\varphi_0}}{\rho_p \omega_p} & \frac{\rho_p}{\omega_p} e^{-i\varphi_0} & -\frac{e^{i\varphi_0}}{\rho_p \omega_p} \\ i \frac{\rho_n}{\omega_n} e^{-i\varphi_0} & i \frac{e^{i\varphi_0}}{\rho_n \omega_n} & -i \frac{\rho_n}{\omega_n} e^{i\varphi_0} & -i \frac{e^{-i\varphi_0}}{\rho_n \omega_n} & -i \frac{\rho_p}{\omega_p} e^{i\varphi_0} & -i \frac{e^{-i\varphi_0}}{\rho_p \omega_p} & i \frac{\rho_p}{\omega_p} e^{-i\varphi_0} & i \frac{e^{i\varphi_0}}{\rho_p \omega_p} \\ \frac{1}{\omega_n} & -\frac{1}{\omega_n} & \frac{1}{\omega_n} & -\frac{1}{\omega_n} & -\frac{1}{\omega_p} & \frac{1}{\omega_p} & -\frac{1}{\omega_p} & \frac{1}{\omega_p} \\ -\frac{i}{\omega_n} & -\frac{i}{\omega_n} & \frac{i}{\omega_n} & \frac{i}{\omega_n} & -\frac{i}{\omega_p} & -\frac{i}{\omega_p} & \frac{i}{\omega_p} & \frac{i}{\omega_p} \\ \rho_n e^{-i\varphi_0} & -\frac{e^{i\varphi_0}}{\rho_n} & -\rho_n e^{i\varphi_0} & \frac{e^{-i\varphi_0}}{\rho_n} & \rho_p e^{i\varphi_0} & -\frac{e^{-i\varphi_0}}{\rho_p} & -\rho_p e^{-i\varphi_0} & \frac{e^{i\varphi_0}}{\rho_p} \\ i \rho_n e^{-i\varphi_0} & i \frac{e^{i\varphi_0}}{\rho_n} & i \rho_n e^{i\varphi_0} & i \frac{e^{-i\varphi_0}}{\rho_n} & -i \rho_p e^{i\varphi_0} & -i \frac{e^{-i\varphi_0}}{\rho_p} & -i \rho_p e^{-i\varphi_0} & -i \frac{e^{i\varphi_0}}{\rho_p} \\ 1 & -1 & -1 & 1 & -1 & 1 & 1 & -1 \\ -i & -i & -i & -i & -i & -i & -i & -i \end{pmatrix}, \quad (\text{B10})$$

with $\varphi_0 = \tan^{-1}(\omega_E, \omega_D)$. Here, ρ_n and ρ_p are expressed collectively as Eq. (25). The columns of \mathcal{V} correspond sequentially to the eigenvectors associated with the frequencies given in the diagonal matrix of the eigenfrequencies Ω for circularly polarized SWs. From \mathcal{V} , we then extract the complex amplitudes of SWs, i.e. \mathcal{A}_θ^e , \mathcal{A}_ϕ^e , \mathcal{A}_θ^o , and \mathcal{A}_ϕ^o . Substituting these amplitudes into the plane-wave solutions in Eq. (14) and taking the real parts yields the explicit expressions for spin-wave excitations, as formulated in Eqs. (22) and (23). All relevant parameters are summarized in Tab. I.

and

$$\mathcal{M}_{21} = \frac{2}{\eta} \begin{pmatrix} \omega_E + \omega_K & 0 & \omega_{ECS} & \omega_{DCS} \\ 0 & \omega_E + \omega_K & \omega_{DCS} & -\omega_{ECS} \\ \omega_{ECS} & \omega_{DCS} & \omega_E + \omega_K & 0 \\ \omega_{DCS} & -\omega_{ECS} & 0 & \omega_E + \omega_K \end{pmatrix}, \quad (\text{B7})$$

where we have introduced $\cos ka = cs$ to shorten the expressions.

After solving Eq. (B4), the eigenfrequencies and eigenvectors can be arranged in matrix form as

$$\mathcal{M}\mathcal{V} = \Omega\mathcal{V}, \quad (\text{B8})$$

where Ω is the diagonal matrix of the eigenvalues, i.e.

$$\Omega = \text{diag}[\omega_n, \omega_n, -\omega_n, -\omega_n, \omega_p, \omega_p, -\omega_p, -\omega_p]. \quad (\text{B9})$$

Here, ω_n and ω_p [unified in Eq. (24)] are the nutational and precessional frequencies, respectively. The eigenvector matrix \mathcal{V} in Eq. (B8) is written as

Appendix C: SW solution in canted configuration

When $\omega_D > \omega_D^c$, the canted configuration [sketched in Fig. 1(c)] is energetically favorable at equilibrium and doubly degenerate. We chose $\mathbf{m}_{2j}^0 = -\cos \phi_c \mathbf{e}_x + \sin \phi_c \mathbf{e}_y$ and $\mathbf{m}_{2j+1}^0 = \cos \phi_c \mathbf{e}_x + \sin \phi_c \mathbf{e}_y$, i.e. $\theta_{2j}^0 = \theta_{2j+1}^0 = \pi/2$, $\phi_{2j}^0 = \pi - \phi_c$, and $\phi_{2j+1}^0 = \phi_c$, with ϕ_c being Eq. (21). Then we combine this equilibrium magnetization with the spin-wave fluctuations in Eq. (4) to obtain the total magnetization. Substituting the resultant expression into the reduced magnetic energy in Eq. (18) for staggered DMI, along with the coordinate transformation given in Eq. (2), one can explicitly calculate all matrices in Eq. (9) as follows: $\mathcal{H}_l = 2 \text{diag}[\omega_E \cos \phi_l^0 -$

$(-1)^l \omega_D \sin \phi_l^0 - \omega_K, \omega_E \cos \phi_l^0 - (-1)^l \omega_D \sin \phi_l^0]$, and $\mathcal{H}_{l\pm 1} = \text{diag}[\omega_E, -\omega_E \cos \phi_l^0 + (-1)^l \omega_D \sin \phi_l^0]$.

Given that the canted configuration possesses the identical magnetic period as the AFM phase, following the routine in Sec. B we obtain the similar spin-wave eigen equation described by Eqs. (B4) and (B5) with

$$\mathcal{M}_{21} = \frac{2}{\eta} \begin{pmatrix} \tilde{\omega}_E - \omega_K & 0 & \omega_{ECS} & 0 \\ 0 & \tilde{\omega}_E & 0 & -\tilde{\omega}_{ECS} \\ \omega_{ECS} & 0 & \tilde{\omega}_E - \omega_K & 0 \\ 0 & -\tilde{\omega}_{ECS} & 0 & \tilde{\omega}_E \end{pmatrix}, \quad (\text{C1})$$

$$\mathcal{V} = \begin{pmatrix} \rho_n^+ & \rho_n^+ & -\rho_n^- & -\rho_n^- & -\rho_p^+ & -\rho_p^+ & \rho_p^- & \rho_p^- \\ -\frac{i}{\omega_n^+} & \frac{i}{\omega_n^+} & \frac{i}{\omega_n^-} & -\frac{i}{\omega_n^-} & -\frac{i}{\omega_p^+} & \frac{i}{\omega_p^+} & \frac{i}{\omega_p^-} & -\frac{i}{\omega_p^-} \\ -\rho_n^+ & -\rho_n^+ & -\rho_n^- & -\rho_n^- & \rho_p^+ & \rho_p^+ & \rho_p^- & \rho_p^- \\ i\frac{1}{\omega_n^+} & -i\frac{1}{\omega_n^+} & i\frac{1}{\omega_n^-} & -i\frac{1}{\omega_n^-} & i\frac{1}{\omega_p^+} & -i\frac{1}{\omega_p^+} & i\frac{1}{\omega_p^-} & -i\frac{1}{\omega_p^-} \\ \rho_n^+ \omega_n^+ & -\rho_n^+ \omega_n^+ & -\rho_n^- \omega_n^- & \rho_n^- \omega_n^- & -\rho_p^+ \omega_p^+ & \rho_p^+ \omega_p^+ & \rho_p^- \omega_p^- & -\rho_p^- \omega_p^- \\ -i & -i & i & i & -i & -i & i & i \\ -\rho_n^+ \omega_n^+ & \rho_n^+ \omega_n^+ & -\rho_n^- \omega_n^- & \rho_n^- \omega_n^- & \rho_p^+ \omega_p^+ & -\rho_p^+ \omega_p^+ & \rho_p^- \omega_p^- & -\rho_p^- \omega_p^- \\ i & i & i & i & i & i & i & i \end{pmatrix}. \quad (\text{C2})$$

Here, ω_n^\pm and ω_p^\pm [unified in Eq. (32)] are the nutational and precessional frequencies, respectively. ρ_n^\pm and ρ_p^\pm are expressed collectively as Eq. (33). The columns of \mathcal{V} correspond sequentially to the eigenvectors associated with the frequencies given in the diagonal matrix of the eigenfrequencies Ω . From \mathcal{V} , we then extract the complex amplitudes of SWs, i.e. \mathcal{A}_θ^e , \mathcal{A}_ϕ^e , \mathcal{A}_θ^o , and \mathcal{A}_ϕ^o . Substituting these amplitudes into the plane-wave solutions in Eq. (14) and taking the real parts yields the explicit expressions for spin-wave excitations, as formulated in Eqs. (22)-(23). All relevant parameters are summarized in Tab. III.

Appendix D: SW solution in homogeneous-DMI antiferromagnetic configuration

Compared with Sec. B, the AFM configuration remains identical, while the DMI term is modified into the staggered form. So, following the same procedure as Sec. B, the matrixes in Eq. (9) can be calculated. \mathcal{H}_l is still $2 \text{diag}[\omega_E + \omega_K, \omega_E + \omega_K]$. $\mathcal{H}_{l\pm 1}$ becomes

$$\mathcal{H}_{l\pm 1} = \begin{pmatrix} \omega_E & \mp \omega_D \cos \phi_l^0 \\ \mp \omega_D \cos \phi_l^0 & -\omega_E \end{pmatrix}. \quad (\text{D1})$$

where $\tilde{\omega}_E = \sqrt{\omega_E^2 + \omega_D^2}$ and $cs = \cos(ka)$.

After solving the spin-wave eigen equation [Eqs. (B4), (B5) and (C1)], all the eigenvalues and corresponding eigenvectors are arranged as $\mathcal{M}\mathcal{V} = \Omega\mathcal{V}$, where \mathcal{M} is the parameter matrix Eq. (B5) with \mathcal{M}_{21} being Eq. (C1), Ω is the diagonal matrix of the eigenvalues, expressed as $\Omega = \text{diag}[\omega_n^+, -\omega_n^+, \omega_n^-, -\omega_n^-, \omega_p^+, -\omega_p^+, \omega_p^-, -\omega_p^-]$, and the eigenvector matrix

Then, the eigen equation for SWs is derived, described by Eqs. (B4) and (B5) with

$$\mathcal{M}_{21} = \frac{2}{\eta} \begin{pmatrix} \omega_E + \omega_K & 0 & \omega_{ECS} & i\omega_D sn \\ 0 & \omega_E + \omega_K & i\omega_D sn & -\omega_{ECS} \\ \omega_{ECS} & -i\omega_D sn & \omega_E + \omega_K & 0 \\ -i\omega_D sn & -\omega_{ECS} & 0 & \omega_E + \omega_K \end{pmatrix}, \quad (\text{D2})$$

with $sn = \sin(ka)$ and $cs = \cos(ka)$. Here, compared with Eq. (B7), only the DMI-related elements are changed.

After solving the spin-wave eigen equation [Eqs. (B4), (B5) and (D2)], all the eigenvalues and corresponding eigenvectors are arranged as $\mathcal{M}\mathcal{V} = \Omega\mathcal{V}$, where \mathcal{M} is the parameter matrix Eq. (B5) with \mathcal{M}_{21} being Eq. (D2), Ω is the diagonal matrix of the eigenvalues, expressed as $\Omega = \text{diag}[\omega_n^+, -\omega_n^+, \omega_n^-, -\omega_n^-, \omega_p^+, -\omega_p^+, \omega_p^-, -\omega_p^-]$, and the eigenvector matrix is written as

$$\mathcal{V} = \begin{pmatrix} \frac{\rho_n^+}{\omega_n^+} & -\frac{1}{\rho_n^+ \omega_n^+} & -\frac{\rho_n^-}{\omega_n^-} & \frac{1}{\rho_n^- \omega_n^-} & -\frac{\rho_p^+}{\omega_p^+} & \frac{1}{\rho_p^+ \omega_p^+} & \frac{\rho_p^-}{\omega_p^-} & -\frac{1}{\rho_p^- \omega_p^-} \\ \frac{i\rho_n^+}{\omega_n^+} & -\frac{i}{\rho_n^+ \omega_n^+} & \frac{i\rho_n^-}{\omega_n^-} & -\frac{i}{\rho_n^- \omega_n^-} & -\frac{i\rho_p^+}{\omega_p^+} & \frac{i}{\rho_p^+ \omega_p^+} & -\frac{i\rho_p^-}{\omega_p^-} & \frac{i}{\rho_p^- \omega_p^-} \\ \frac{1}{\omega_n^+} & -\frac{1}{\omega_n^+} & -\frac{1}{\omega_n^-} & \frac{1}{\omega_n^-} & \frac{1}{\omega_p^+} & -\frac{1}{\omega_p^+} & -\frac{1}{\omega_p^-} & \frac{1}{\omega_p^-} \\ -\frac{i}{\omega_n^+} & \frac{i}{\omega_n^+} & -\frac{i}{\omega_n^-} & \frac{i}{\omega_n^-} & -\frac{i}{\omega_p^+} & \frac{i}{\omega_p^+} & -\frac{i}{\omega_p^-} & \frac{i}{\omega_p^-} \\ \rho_n^+ & \frac{1}{\rho_n^+} & -\rho_n^- & -\frac{1}{\rho_n^-} & -\rho_p^+ & -\frac{1}{\rho_p^+} & \rho_p^- & \frac{1}{\rho_p^-} \\ i\rho_n^+ & \frac{i}{\rho_n^+} & i\rho_n^- & \frac{i}{\rho_n^-} & -i\rho_p^+ & -\frac{i}{\rho_p^+} & -i\rho_p^- & -\frac{i}{\rho_p^-} \\ 1 & 1 & -1 & -1 & 1 & 1 & -1 & -1 \\ -i & -i & -i & -i & -i & -i & -i & -i \end{pmatrix}. \quad (\text{D3})$$

Here, ω_n^\pm and ω_p^\pm , unified in Eq. (48), denote the nutational and precessional frequencies, respectively, while ρ_n^\pm and ρ_p^\pm are collectively given by Eq. (49). The columns of \mathcal{V} sequentially correspond to the eigenvectors associated with the frequencies listed in the diagonal eigenfrequency matrix Ω . From \mathcal{V} , we then extract the complex spin-wave amplitudes, \mathcal{A}_θ^e , \mathcal{A}_ϕ^e , \mathcal{A}_θ^o , and \mathcal{A}_ϕ^o . Substituting these amplitudes into the plane-wave solutions in Eq. (14) and taking the real parts yields the explicit expressions for the spin-wave excitations, as given in Eqs. (22) and (23). The relevant parameters are summarized in Tab. IV.

Appendix E: SW solution in spiral configuration

When $\omega_D > \omega_D^c$, the static configuration is spiral under homogeneous DMI, as schematically displayed in Fig. 1(b). The magnetization in equilibrium reads $\mathbf{m}_l^0 = \cos(l\phi_s)\mathbf{e}_x + \sin(l\phi_s)\mathbf{e}_y$.

We then combine this equilibrium magnetization with the spin-wave fluctuations in Eq. (4) to obtain the total magnetization. Substituting the resulting expression into the reduced magnetic energy for homogeneous DMI in Eq. (18), together with the coordinate transformation in Eq. (2), allows all matrices in Eq. (9) to be calculated explicitly as follows: $\mathcal{H}_l = -2 \text{diag}[\omega_K + \omega_E \cos \phi_s + \omega_D \sin \phi_s, \omega_E \cos \phi_s + \omega_D \sin \phi_s]$, and $\mathcal{H}_{l\pm 1} = \text{diag}[\omega_E, \omega_E \cos \phi_s + \omega_D \sin \phi_s]$, where the helical angle ϕ_s is Eq. (20).

Next, the parameter matrixes \mathcal{M}_l and $\mathcal{M}_{l\pm 1}$ in Eq. (15) can be constructed using \mathcal{H}_l and $\mathcal{H}_{l\pm 1}$, as well as Eqs. (8), (12) and (13). It should be noted that \mathcal{H}_l and $\mathcal{H}_{l\pm 1}$ are independent of the site location l . Therefore, after calculating the parameter matrixes \mathcal{M}_l and $\mathcal{M}_{l\pm 1}$,

Eq. (15) becomes

$$\mathcal{M} \begin{pmatrix} \mathcal{A}_\theta \\ \mathcal{A}_\phi \\ \omega \mathcal{A}_\theta \\ \omega \mathcal{A}_\phi \end{pmatrix} = \omega \begin{pmatrix} \mathcal{A}_\theta \\ \mathcal{A}_\phi \\ \omega \mathcal{A}_\theta \\ \omega \mathcal{A}_\phi \end{pmatrix}, \quad (\text{E1})$$

where the parameter matrix read

$$\mathcal{M} = \frac{1}{\eta} \begin{pmatrix} 0 & 0 & \eta & 0 \\ 0 & 0 & 0 & \eta \\ 2(\tilde{\omega}_E - \omega_K + \omega_E cs) & 0 & 0 & i \\ 0 & 2\tilde{\omega}_E(1 - cs) & -i & 0 \end{pmatrix}, \quad (\text{E2})$$

with $\tilde{\omega}_E = \sqrt{\omega_E^2 + \omega_D^2}$ and $cs = \cos(ka)$.

After solving these linearized equations [Eq. (E1)], all the eigenvalues and corresponding eigenvectors are arranged as $\mathcal{M}\mathcal{V} = \Omega\mathcal{V}$, where Ω is the diagonal matrix of the eigenvalues, expressed as $\Omega = \text{diag}[\omega_n, -\omega_n, \omega_p, -\omega_p]$, and the eigenvector matrix is given by

$$\mathcal{V} = \begin{pmatrix} -\rho_n & -\rho_n & \rho_p & \rho_p \\ \frac{i}{\omega_n} & -\frac{i}{\omega_n} & \frac{i}{\omega_p} & -\frac{i}{\omega_p} \\ -\rho_n \omega_n & \rho_n \omega_n & \rho_p \omega_p & -\rho_p \omega_p \\ i & i & i & i \end{pmatrix}. \quad (\text{E3})$$

Here, $\omega_{n,p}$ are $\omega_{n,p}^-$ in Eq. (32), and $\rho_{n,p}$ are $\rho_{n,p}^-$ in Eq. (33). The columns of \mathcal{V} correspond, in order, to the eigenvectors associated with the frequencies listed in the diagonal eigenfrequency matrix Ω . The site-independent complex spin-wave amplitudes \mathcal{A}_θ and \mathcal{A}_ϕ are then extracted from \mathcal{V} . Substituting these amplitudes into the plane-wave solutions in Eq. (14) and taking the real parts yields the explicit spin-wave excitations given in Eq. (16). The relevant parameters are summarized in Tab. VI.

-
- [1] Ritwik Mondal, Levente Rózsa, Michael Farle, Peter M. Oppeneer, Ulrich Nowak, Mikhail Cherkasskii, Inertial effects in ultrafast spin dynamics, *J. Magn. Magn. Mater.* **579**, 170830 (2023).
- [2] Kumar Neeraj, Nilesh Awari, Sergey Kovalev, Debanjan Polley, Nanna Zhou Hagström, Sri Sai Phani Kanth Arekapudi, Anna Semisalova, Kilian Lenz, Bertram Green, Jan-Christoph Deinert, Igor Ilyakov, Min Chen, Mohammed Bawatna, Valentino Scalera, Massimiliano d'Aquino, Claudio Serpico, Olav Hellwig, Jean-Eric Wegrowe, Michael Gensch, and Stefano Bonetti, Inertial spin dynamics in ferromagnets, *Nat. Phys.* **17**, 245 (2021).
- [3] Vivek Unikandanunni, Rajasekhar Medapalli, Marco Asa, Edoardo Albisetti, Daniela Petti, Riccardo Bertacco, Eric E. Fullerton, and Stefano Bonetti, Inertial spin dynamics in epitaxial cobalt films, *Phys. Rev. Lett.* **129**, 237201 (2022).
- [4] Anulekha De, Julius Schlegel, Akira Lentfert, Laura Scheuer, Benjamin Stadtmüller, Philipp Pirro, Georg von Freymann, Ulrich Nowak, and Martin Aeschlimann, Magnetic nutation: Transient separation of magnetization from its angular momentum, *Phys. Rev. B* **111**, 014432 (2025).
- [5] M.-C. Ciornei, J. M. Rubí, and J.-E. Wegrowe, Magnetization dynamics in the inertial regime: Nutation predicted at short time scales, *Phys. Rev. B* **83**, 020410(R) (2011).
- [6] J.-E. Wegrowe and M.-C. Ciornei, Magnetization dynamics, gyromagnetic relation, and inertial effects, *Am. J. Phys.* **80**, 607 (2012).
- [7] Stefano Giordano and Pierre-Michel Déjardin, Derivation of magnetic inertial effects from the classical mechanics of a circular current loop, *Phys. Rev. B* **102**, 214406 (2020).
- [8] Harry Suhl, Theory of the magnetic damping constant, *IEEE Trans. Magn.* **34**, 1834 (1998).
- [9] Manfred Fähnle, Daniel Steiauf, and Christian Illg, Generalized Gilbert equation including inertial damping: Derivation from an extended breathing Fermi surface model, *Phys. Rev. B* **84**, 172403 (2011).
- [10] Satadeep Bhattacharjee, Lars Nordstöm, and Jonas Fransson, Atomistic Spin Dynamic Method with both Damping and Moment of Inertia Effects Included from First Principles, *Phys. Rev. Lett.* **108**, 057204 (2012).
- [11] Toru Kikuchi and Gen Tatara, Spin dynamics with inertia in metallic ferromagnets, *Phys. Rev. B* **92**, 184410 (2015).
- [12] Pascal Thibaudeau and Stam Nicolis, Emerging magnetic nutation, *Eur. Phys. J. B* **94**, 196 (2021).
- [13] J. Anders, C. R. J. Sait, and S. A. R. Horsley, Quantum Brownian motion for magnets, *New J. Phys.* **24** 033020 (2022).
- [14] Fuming Xu, Gaoyang Li, Jian Chen, Zhizhou Yu, Lei Zhang, Baigeng Wang, and Jian Wang, Unified framework of the microscopic Landau-Lifshitz-Gilbert equation and its application to skyrmion dynamics, *Phys. Rev. B* **108**, 144409 (2023).
- [15] Utkarsh Bajpai and Branislav K. Nikolić, Time-retarded damping and magnetic inertia in the Landau-Lifshitz-Gilbert equation self-consistently coupled to electronic time-dependent nonequilibrium Green functions, *Phys. Rev. B* **99**, 134409 (2019).
- [16] Christian Svingen Johnsen and Asle Sudbø, Dynamically generated spin interactions and nutational spin inertia in normal metal-ferromagnet heterostructures, *Phys. Rev. B* **111**, 144423 (2025).
- [17] Mario Gaspar Quarenta, Mithuss Tharmalingam, Tim Ludwig, H. Y. Yuan, Lukasz Karwacki, Robin C. Verstraten, and Rembert A. Duine, Bath-Induced Spin Inertia, *Phys. Rev. Lett.* **133**, 136701 (2024).
- [18] Ritwik Mondal, Marco Berritta, Ashis K. Nandy, and Peter M. Oppeneer, Relativistic theory of magnetic inertia in ultrafast spin dynamics, *Phys. Rev. B* **96**, 024425 (2017).
- [19] Ritwik Mondal, Marco Berritta, and Peter M Oppeneer, Generalisation of Gilbert damping and magnetic inertia parameter as a series of higher-order relativistic terms, *J. Phys.: Condens. Matter* **30**, 265801 (2018).
- [20] Felipe Reyes-Osorio and Branislav K. Nikolić, Optically Induced Magnetic Inertia and Magnons from Non-Markovian Extension of the Landau-Lifshitz-Gilbert Equation, *Phys. Rev. Lett.* **135**, 246701 (2025).
- [21] S. V. Titov, W. T. Coffey, Yu. P. Kalmykov, and M. Zarifakis, Deterministic inertial dynamics of the magnetization of nanoscale ferromagnets, *Phys. Rev. B* **103**, 214444 (2021).
- [22] D. Böttcher, and J. Henk, Significance of nutation in magnetization dynamics of nanostructures, *Phys. Rev. B* **86**, 020404(R) (2012).
- [23] Sergei V. Titov, William J. Dowling, Anton S. Titov, Sergey A. Nikitov, and Mikhail Cherkasskii, Inertial dynamics and equilibrium correlation functions of magnetization at short times, *Phys. Rev. B* **107**, 104416 (2023).
- [24] E. Olive, Y. Lansac, and J.-E. Wegrowe, Beyond ferromagnetic resonance: The inertial regime of the magnetization, *Appl. Phys. Lett.* **100**, 192407 (2012).
- [25] E. Olive, Y. Lansac, M. Meyer, M. Hayoun, and J.-E. Wegrowe, Deviation from the Landau-Lifshitz-Gilbert equation in the inertial regime of the magnetization, *J. Appl. Phys.* **117**, 213904 (2015).
- [26] Mikhail Cherkasskii, Michael Farle, and Anna Semisalova, Nutation resonance in ferromagnets, *Phys. Rev. B* **102**, 184432 (2020).
- [27] Ritwik Mondal, Theory of magnetic inertial dynamics in two-sublattice ferromagnets, *J. Phys.: Condens. Matter* **33** 275804 (2021).
- [28] Sergei V. Titov, William J. Dowling, and Yuri P. Kalmykov, Ferromagnetic and nutation resonance frequencies of nanomagnets with various magnetocrystalline anisotropies, *J. Appl. Phys.* **131**, 193901 (2022).
- [29] Mikhail Cherkasskii, Igor Barsukov, Ritwik Mondal, Michael Farle, and Anna Semisalova, Theory of inertial spin dynamics in anisotropic ferromagnets, *Phys. Rev. B* **106**, 054428 (2022).
- [30] Subhadip Ghosh, Mikhail Cherkasskii, Igor Barsukov, and Ritwik Mondal, Theory of tensorial magnetic inertia in terahertz spin dynamics, *Phys. Rev. B* **110**, 174430 (2024).
- [31] Jonas Wiemeler, Michael Farle, and Anna S. Semisalova, High-frequency susceptibility tensor in the inertial regime: Prediction for subterahertz magnonics in ferromagnets, *Phys. Rev. B* **112**, 094433 (2025).
- [32] Ritwik Mondal, Sebastian Großenbach, Levente Rózsa,

- and Ulrich Nowak, Nutation in antiferromagnetic resonance, *Phys. Rev. B* **103**, 104404 (2021).
- [33] Ritwik Mondal and Peter M. Oppeneer, Influence of intersublattice coupling on the terahertz nutation spin dynamics in antiferromagnets, *Phys. Rev. B* **104**, 104405 (2021).
- [34] David Angster, Tobias Dannegger, Julius Schlegel, Martin Evers, and Ulrich Nowak, Nutational resonance modes in antiferromagnetic materials, *Sci. Rep.* **15**, 21543 (2025).
- [35] Ritwik Mondal, and Akashdeep Kamra, Spin pumping at terahertz nutation resonances, *Phys. Rev. B* **104**, 214426 (2021).
- [36] Peng-Bin He, Ri-Xing Wang, Zai-Dong Li, and Mikhail Cherkasskii, Chirality and polarization of inertial antiferromagnetic resonances driven by spin-orbit torques, *Phys. Rev. B* **112**, 224423 (2025).
- [37] Peng-Bin He, Large-amplitude and widely tunable self-oscillations enabled by the inertial effect in uniaxial antiferromagnets driven by spin-orbit torques, *Phys. Rev. B* **108**, 184418 (2023).
- [38] Peng-Bin He, Influence of the magnetic inertia on the self-oscillation in spin-orbit torque-driven tripartite antiferromagnets with a 120° rotation symmetry, *Phys. Rev. B* **110**, 064411 (2024).
- [39] Rodolfo Rodriguez, Mikhail Cherkasskii, Rundong Jiang, Ritwik Mondal, Arezoo Etesamirad, Allison Tossounian, Boris A. Ivanov, and Igor Barsukov, Spin Inertia and Auto-Oscillations in Ferromagnets, *Phys. Rev. Lett.* **132**, 246701 (2024).
- [40] Rahnema Rahman and Supriyo Bandyopadhyay, An observable effect of spin inertia in slow magneto-dynamics: increase of the switching error rates in nanoscale ferromagnets, *J. Phys.: Condens. Matter* **33** 355801 (2021).
- [41] Kumar Neeraj, Matteo Pancaldi, Valentino Scalera, Salvatore Perna, Massimiliano d'Aquino, Claudio Serpico, and Stefano Bonetti, Magnetization switching in the inertial regime, *Phys. Rev. B* **105**, 054415 (2022).
- [42] I. Makhfudz, Y. Hajati, and E. Olive, High-temperature magnetization reversal in the inertial regime, *Phys. Rev. B* **106**, 134415 (2022).
- [43] Lucas Winter, Sebastian Großenbach, Ulrich Nowak, and Levente Rózsa, Nutational switching in ferromagnets and antiferromagnets, *Phys. Rev. B* **106**, 214403 (2022).
- [44] I. Makhfudz, E. Olive, and S. Nicolis, Nutation wave as a platform for ultrafast spin dynamics in ferromagnets, *Appl. Phys. Lett.* **117**, 132403 (2020).
- [45] Mikhail Cherkasskii, Michael Farle, and Anna Semislova, Dispersion relation of nutation surface spin waves in ferromagnets, *Phys. Rev. B* **103**, 174435 (2021).
- [46] Alexey M. Lomonosov, Vasily V. Temnov, and Jean-Eric Wegrowe, Anatomy of inertial magnons in ferromagnetic nanostructures, *Phys. Rev. B* **104**, 054425 (2021).
- [47] Sergei V. Titov, William J. Dowling, Yuri P. Kalmykov, and Mikhail Cherkasskii, Nutation spin waves in ferromagnets, *Phys. Rev. B* **105**, 214414 (2022).
- [48] Ritwik Mondal, and Levente Rózsa, Inertial spin waves in ferromagnets and antiferromagnets, *Phys. Rev. B* **106**, 134422 (2022).
- [49] Mikhail Cherkasskii, Ritwik Mondal, and Levente Rózsa, Inertial spin waves in spin spirals, *Phys. Rev. B* **109**, 184424 (2024).
- [50] Peng-Bin He and Mikhail Cherkasskii, Temporal and spatial attenuation of inertial spin waves driven by spin-transfer torques, *Phys. Rev. B* **110**, 174431 (2024).
- [51] Massimiliano d'Aquino, and Riccardo Hertel, Nonreciprocal Inertial Spin-Wave Dynamics in Twisted Magnetic Nanostrips, *Phys. Rev. Lett.* **135**, 216705 (2025).
- [52] H. Y. Yuan, Using surface plasmons to detect spin inertia, *Phys. Rev. B* **112**, 054438 (2025).
- [53] Subhadip Ghosh, Darpa Narayan Basu, and Ritwik Mondal, Engineering spin-wave spectrum via the magnetization inertia tensor, *J. Phys.: Condens. Matter* **38**, 015803 (2026).
- [54] D. H. Goldstein, *Polarized light*, (CRC Press, Taylor & Francis Group, 2011), p. 57.
- [55] I. Dzyaloshinskii, A thermodynamic theory of “weak” ferromagnetism of antiferromagnetics, *J. Phys. Chem. Solids* **4**, 241 (1958).
- [56] Tôru Moriya, Anisotropic Superexchange Interaction and Weak Ferromagnetism, *Phys. Rev.* **120**, 91 (1960).
- [57] J. H. H. Perk and H. W. Capel, Antisymmetric exchange, canting and spiral structure, *Phys. Lett. A* **58**, 115 (1976).
- [58] Carmine Autieri, Raghottam M. Sattigeri, Giuseppe Cuono, and Amar Fakhredine, Staggered Dzyaloshinskii-Moriya interaction inducing weak ferromagnetism in centrosymmetric altermagnets and weak ferrimagnetism in noncentrosymmetric altermagnets, *Phys. Rev. B* **111**, 054442 (2025).
- [59] Xiyin Ye, Qirui Cui, Weiwei Lin, and Tao Yu, Spin quenching and transport by hidden Dzyaloshinskii-Moriya interactions, *Phys. Rev. B* **111**, 064401 (2025).
- [60] Wolfram Research (1988), ArcTan, Wolfram Language function, <https://reference.wolfram.com/language/ref/ArcTan.html> (updated 2021).
- [61] Sergio M. Rezende, Antonio Azevedo, and Roberto L. Rodríguez-Suárez, Introduction to antiferromagnetic magnons, *J. Appl. Phys.* **126**, 151101 (2019).
- [62] Priyanka Vaidya, Sophie A. Morley, Johan van Tol, Yan Liu, Ran Cheng, Arne Brataas, David Lederman, and Enrique del Barco, Subterahertz spin pumping from an insulating antiferromagnet, *Science* **368**, 160 (2020).
- [63] Z. Q. Qiu, Chirality dependence of spin current in spin pumping, *Nat. Commun.* **13**, 5229 (2022).
- [64] Yutian Wang, Jiongjie Wang, Ruoban Ma, and Jiang Xiao, Connection between spin-wave polarization and dissipation, *Phys. Rev. B* **111**, 134431 (2025).
- [65] Taku J Sato and Kittiwit Matan, Nonreciprocal Magnons in Noncentrosymmetric Magnets, *J. Phys. Soc. Jpn.* **88**, 081007 (2019).
- [66] J. J. Sakurai, *Modern Quantum Mechanics*, Revised edition (Addison-Wesley, 1994), pp. 30-41.
- [67] Roald Hoffmann, *Solids and Surfaces: A Chemist's View of Bonding in Extended Structures* (Wiley-VCH, 1988), pp. 83-90.
- [68] R. W. Damon and J. R. Eshbach, *J. Phys. Chem. Solids* **19**, 308 (1961).